

## FORMATION OF MASSIVE PRIMORDIAL STARS: INTERMITTENT UV FEEDBACK WITH EPISODIC MASS ACCRETION

TAKASHI HOSOKAWA<sup>1,2</sup>, SHINGO HIRANO<sup>2</sup>, ROLF KUIPER<sup>3</sup>, HAROLD W. YORKE<sup>4</sup>,  
KAZUYUKI OMUKAI<sup>5</sup>, NAOKI YOSHIDA<sup>2,6</sup>

*Draft version September 6, 2018*

### ABSTRACT

We present coupled stellar evolution (SE) and 3D radiation-hydrodynamic (RHD) simulations of the evolution of primordial protostars, their immediate environment, and the dynamic accretion history under the influence of stellar ionizing and dissociating UV feedback. Our coupled SE-RHD calculations result in a wide diversity of final stellar masses covering  $10 M_{\odot} \lesssim M_{*} \lesssim 10^3 M_{\odot}$ . The formation of very massive ( $\gtrsim 250 M_{\odot}$ ) stars is possible under weak UV feedback, whereas ordinary massive (a few  $\times 10 M_{\odot}$ ) stars form when UV feedback can efficiently halt the accretion. This may explain the peculiar abundance pattern of a Galactic metal-poor star recently reported by Aoki et al. (2014), possibly the observational signature of very massive precursor primordial stars. Weak UV feedback occurs in cases of variable accretion, in particular when repeated short accretion bursts temporarily exceed  $0.01 M_{\odot} \text{ yr}^{-1}$ , causing the protostar to inflate. In the bloated state, the protostar has low surface temperature and UV feedback is suppressed until the star eventually contracts, on a thermal adjustment timescale, to create an HII region. If the delay time between successive accretion bursts is sufficiently short, the protostar remains bloated for extended periods, initiating at most only short periods of UV feedback. Disk fragmentation does not necessarily reduce the final stellar mass. Quite the contrary, we find that disk fragmentation enhances episodic accretion as many fragments migrate inward and are accreted onto the star, thus allowing continued stellar mass growth under conditions of intermittent UV feedback. This trend becomes more prominent as we improve the resolution of our simulations. We argue that simulations with significantly higher resolution than reported previously are needed to derive accurate gas mass accretion rates onto primordial protostars.

*Subject headings:* cosmology: theory – early universe – galaxies: formation – stars: formation – accretion

### 1. INTRODUCTION

Modern cosmology predicts that the early universe is dominated by massive ( $M_{*} \gtrsim 10 M_{\odot}$ ) primordial stars (e.g., Bromm et al. 2009; Greif 2015). The formation of such massive primordial stars is thought to begin in mini-haloes at  $z \simeq 20 - 30$  (e.g., Abel et al. 2002; Yoshida et al. 2003), forming tiny embryo protostars ( $M_{*} \sim 10^{-2} M_{\odot}$ ) after the gravitational collapse of natal clouds (e.g., Omukai & Nishi 1998; Yoshida et al. 2008). These protostars grow in mass by accreting surrounding gas (e.g., Omukai & Palla 2003; Tan & McKee 2004). Their evolution in the accretion stage and how they interact with their environment determine the characteristics of the emerging massive stars.

Recent theoretical studies suggest that the typical final stellar mass will be somewhat smaller than that of the cloud mass,  $\sim 10^3 M_{\odot}$  (e.g., Bromm et al. 2002).

Stellar radiative feedback is one of the crucial processes which regulate the mass accretion (e.g., Omukai & Inutsuka 2002; McKee & Tan 2008). Hosokawa et al. (2011, 2012b, hereafter HS11 and HS12) show that, with coupled stellar evolution (SE) and 2D axisymmetric radiation-hydrodynamic (RHD) simulations, UV feedback eventually halts the accretion of material onto the protostar. As the stellar UV emissivity rises with increasing stellar mass, a bipolar HII region forms and dynamically expands, first slowing, then reversing the inward flow of gas in the accretion envelope. The circumstellar accretion disk also loses gas via photoevaporation, being exposed to the stellar UV radiation. Hirano et al. (2014, hereafter HR14) have greatly extended the above work to follow the evolution in more than one hundred primordial clouds taken from 3D cosmological simulations. Although UV feedback eventually shuts off mass accretion in general, the resulting final stellar masses have great diversity, spanning  $10 M_{\odot} \lesssim M_{*} \lesssim 10^3 M_{\odot}$  (see also Susa et al. 2014; Hirano et al. 2015, hereafter HR15).

Whereas the 2D simulations have revealed the dynamic nature of stellar UV feedback, 3D simulations show an additional aspect of mass accretion through self-gravitating circumstellar disks (e.g., Stacy et al. 2010; Clark et al. 2011; Greif et al. 2011, 2012; Vorobyov et al. 2013; Machida & Doi 2013). In particular, these studies show that disks readily fragment via gravitational instability. The fate of the fragments seems to have a great diversity; some will survive, being expelled from the system via gravitational ejection, and others will migrate inward

<sup>1</sup> Research Center for the Early Universe, the University of Tokyo, Tokyo 113-0033, Japan; takashi.hosokawa@phys.s.u-tokyo.ac.jp, hosokwtk@gmail.com

<sup>2</sup> Department of Physics, School of Science, the University of Tokyo, Tokyo 113-0033, Japan

<sup>3</sup> University of Tübingen, Institute of Astronomy and Astrophysics, Auf der Morgenstelle 10, D-72076 Tübingen, Germany

<sup>4</sup> Jet Propulsion Laboratory, California Institute of Technology, Pasadena CA 91109, USA

<sup>5</sup> Astronomical Institute, Tohoku University, Sendai 980-8578, Japan

<sup>6</sup> Kavli Institute for the Physics and Mathematics of the Universe (WPI), Todai Institutes for Advanced Study, the University of Tokyo, Chiba 277-8583, Japan

through the disk to merge with each other or fall onto the central star causing accretion bursts. Through such recurrent merger and ejection events, binary or multiple stellar systems will finally appear (e.g., Stacy & Bromm 2013).

The final stellar mass should ultimately be determined by the complex interplay between UV feedback and the various 3D effects described above. Performing SE-RHD simulations including all of these effects is still challenging, but nevertheless remains the ultimate goal for computational studies. Whereas the first 3D simulations mostly focused on the early evolution for  $10 - 10^3$  years after the birth of the protostar, Stacy et al. (2012) follow for longer periods ( $\simeq 5 \times 10^3$  years), namely until UV feedback begins to operate. They show that a bipolar HII region grows from a binary system formed via disk fragmentation. Susa (2013) and Susa et al. (2014) follow for even longer periods ( $\simeq 10^5$  years) of evolution, including the effect of photodissociating (FUV) feedback with their 3D simulations, and show that mass accretion onto the star is ultimately halted by the feedback effects.

The above studies suggest that both UV feedback and disk fragmentation might co-operatively reduce the final stellar masses. This is because the accreting gas is divided among multiple protostars and the accretion rates onto each protostar is correspondingly reduced (e.g., Peters et al. 2010). In fact, the mass spectrum derived by Susa et al. (2014) covers a somewhat lower mass range than the 2D results in HR14.

In this paper, we cast a new light on a different mode of interplay between UV feedback and mass accretion in 3D. As described above, highly variable time-dependent mass accretion histories are commonly seen in 3D numerical simulations. Even if the disk undergoes fragmentation, a large fraction of the fragments do not actually survive. For instance, Greif et al. (2012) show that about 2/3 of the emerging fragments eventually merge with other fragments or existing stars. This is driven by the inward migration of the fragments due to strong gravitational torques caused by the asymmetric disk structure (e.g., spiral arms). As a result, accretion histories normally become highly variable, resulting in short accretion bursts followed by relatively long quiescent phases (e.g., Smith et al. 2012; Vorobyov et al. 2013; DeSouza & Basu 2015).

Stellar evolution calculations which include the effects of mass accretion show that rapid accretion with  $\dot{M}_* \gtrsim 10^{-2} M_\odot \text{ yr}^{-1}$  dramatically changes the protostellar structure, causing the abrupt expansion of the star (e.g., Hosokawa et al. 2012a, 2013; Schleicher et al. 2013). Since a star's UV emissivity strongly varies with its effective temperature or radius, the resulting UV feedback expected for accretion bursts potentially show a new feature during the accretion phase.

Here, we present the results of coupled SE-RHD numerical simulations (SE in 1D; RHD in 3D) to follow the stellar growth and evolution with variable mass accretion, including the effects of stellar UV feedback. As in our previous studies HS11 and HR14, we employ a stellar evolution code to numerically solve the interior structure under the assumption of spherical symmetry and mass accretion. We follow the long-term ( $\sim 10^5$  years) evolution of the surrounding gas including the effects of both the hydrogen-ionizing (EUV:  $h\nu \geq 13.6$  eV)

and hydrogen-photodissociating (FUV:  $11.2 \text{ eV} \leq h\nu \leq 13.6$  eV) feedback. As shown below, our current calculations suggest a wide range of final stellar masses, analogous to the results of previous studies (e.g., HR14, HR15; Susa et al. 2014). We show that, as in previous studies, UV feedback can efficiently halt mass accretion for ordinary massive ( $M_* \lesssim 100 M_\odot$ ) stars. On the other hand, it is also possible to form very massive ( $\gtrsim 250 M_\odot$ ) stars, whose observational signature might have been discovered in the Galactic metal-poor star SDSS J001820.5-093939. (Aoki et al. 2014). In direct contrast to popular belief, disk fragmentation does not necessarily reduce the final stellar mass; episodic accretion and/or successive mergers can actually enhance stellar mass growth. For these cases, the rapid and sometimes extreme evolution of the stellar radius with variable mass accretion causes the recurrent extinction and formation of HII regions. Such intermittent UV feedback does not efficiently halt gas accretion onto the protostar until very massive stars finally form. We also stress that performing the stellar evolution calculations together with 3D RHD simulations in realtime enables us to follow the evolution consistently. This is an essential feature of our SE-RHD code.

The rest of the paper is organized as follows. We first describe the numerical methods and the cases considered in Sections 2 and 3. The main results are presented in Section 4. We discuss the implications of our results in Section 5 and summarize our conclusions in Section 6.

## 2. NUMERICAL METHOD

The evolution in the protostellar accretion stage is followed with a hybrid SE-RHD code by solving the 3D RHD of the accretion flow in the vicinity of a protostar simultaneously with the evolution of the protostar inside a sink cell of the RHD grid. This approach is basically the same as that developed by HS11. The dynamics of the accretion flow are followed by performing a 3D RHD simulation, whereby for each time step the characteristics of the protostar (mass, radius, intrinsic luminosity, accretion luminosity, FUV flux, EUV flux) provide boundary conditions for the RHD code at the inner edge of the sink cell, necessary for the radiation transfer, heating/cooling and chemistry modules of the RHD code. The RHD simulation in turn provides the time-dependent mass accretion rate into the sink cell. The protostar's evolution is calculated by numerically solving the interior structure with the additional feature of mass accretion onto the stellar surface (e.g., Kuiper & Yorke 2013; Vorobyov & Basu 2015). We describe the methodologies for the RHD simulations and for stellar evolution calculations in Sections 2.1 and 2.2 respectively.

### 2.1. Radiation Hydrodynamics of Accretion Flow

#### 2.1.1. Simulation Overview and Numerical Configuration

We use a modified version of the public multi-dimensional magneto-hydrodynamics code PLUTO 3.0 (Mignone et al. 2007). The original code had been modified to study present-day high-mass star formation by implementing the sink cell philosophy with the embedded stellar evolution code outlined above, as well as self-gravity and radiation transfer modules (e.g., Kuiper et al. 2010b,a, 2011; Kuiper & Klessen 2013). For this investigation we added several physics modules necessary to study primordial star formation.

Table 1. Cosmological Cases Considered

Cases	$N_R \cdot N_\theta \cdot N_\phi$	$r_{\max}$ ( $10^4$ AU)	$M_{\text{g,tot}}$ ( $M_\odot$ )	$\Delta t$ ( $10^4$ yr)	$M_{*,3\text{D}}$ ( $M_\odot$ )	$M_{*,2\text{D}}$ ( $M_\odot$ )
A	96 · 32 · 64	150	$1.0 \times 10^4$	7	462.4*	751.3
B	96 · 32 · 64	150	$1.3 \times 10^4$	7	598.8*	283.9
B-NF <sup>†</sup>	96 · 32 · 64	150		7		
B-NF-HR2 <sup>‡</sup> -m0*	128 · 64 · 128	4	$1.1 \times 10^3$	0.3		
B-NF-HR2-m40	128 · 64 · 128	4		0.3		
B-NF-HR2-m70	128 · 64 · 128	4		0.3		
B-NF-HR2-m120	128 · 64 · 128	4		0.3		
B-NF-HR4 <sup>‡</sup> -m20	192 · 128 · 256	0.67		0.1		
B-NF-HR4-m20-fc <sup>◊</sup>	192 · 128 · 256	0.67		0.1		
B-NF-HR4-m20-lsk <sup>•</sup>	192 · 128 · 256	0.67		0.1		
C	64 · 32 · 64	4	$1.0 \times 10^3$	12	286.0	160.3
C-HR2-m0	128 · 64 · 128	4		5.5		
D	64 · 32 · 64	4	490	8	67.4	55.5
D-NF	64 · 32 · 64	4		8		
D-DF <sup>†</sup>	64 · 32 · 64	4		8		
E	96 · 32 · 64	150	$2.7 \times 10^3$	6	14.3	24.4

Col. 2: cell numbers, Col. 3: position of the radial outer boundary, Col. 4: total mass contained in the computational domain, Col. 5: time duration followed Col. 6: final stellar masses in the current work, Col. 7: final stellar masses obtained in 2D SE-RHD simulations (Hirano et al. 2014)

\*: Stellar masses at the end of the simulations,  $t = 7 \times 10^4$  years.

†: Suffix “NF” represent casess with no UV feedback and “DF” with only dissociation (FUV) feedback.

‡: Suffix “HR2” represents cases with doubled and “HR4” with quadrupled spatial resolutions.

\*: Suffix “mX” represents the points for the restart after doubling the resolution when  $M_* \simeq X M_\odot$ .

◊: Stringent limit for the cooling with  $f_{\text{limit}} = 24$  (see Section 2.1.2).

•: Larger sink cell with  $r_{\min} \simeq 52$  AU ( $r_{\min} = 30$  AU for all other cases).

The governing equations of hydrodynamics are

$$\frac{\partial \rho}{\partial t} + \nabla \cdot (\rho \mathbf{v}) = 0, \quad (1)$$

$$\frac{\partial(\rho \mathbf{v})}{\partial t} + \nabla \cdot (\rho \mathbf{v} \otimes \mathbf{v}) = -\rho \nabla \Phi - \nabla p, \quad (2)$$

$$\frac{\partial e}{\partial t} + \nabla \cdot (e \mathbf{v}) = -p \nabla \cdot \mathbf{v} + \Gamma - \Lambda, \quad (3)$$

$$p = (\gamma - 1)e, \quad (4)$$

where  $\rho$  and  $p$  are the gas mass density and pressure,  $\mathbf{v}$  the 3D velocity vector,  $\Phi$  the gravitational potential,  $e$  the gas thermal energy density,  $\Gamma$  and  $\Lambda$  the heating and cooling rates per volume respectively. We allow the adiabatic exponent  $\gamma$  to vary depending on the chemical abundances and gas temperature (e.g., Omukai & Nishi 1998). We calculate the energy source term  $\Gamma - \Lambda$  with the same thermal processes as considered in HS11 (Table S1 in HS11, but see Section 2.1.3 below for some differences). Note that equation (2) does not include the viscosity terms which enabled angular momentum transport under 2D axial symmetry (e.g.,  $\alpha$ -viscosity, Shakura & Sunyaev 1973). Instead, gravitational torques induced by the non-axisymmetric disk structure (e.g., spiral arms, clumps) operate in 3D.

As in Kuiper et al. (2011), we solve the above equations in spherical coordinates. The spatial grids for the polar ( $\theta$ ) and azimuthal ( $\phi$ ) directions are homogeneously distributed over  $0 \leq \theta \leq \pi$  and  $0 \leq \phi \leq 2\pi$ . The angular resolutions are thus  $\Delta\theta = \pi/N_\theta$  and  $\Delta\phi = 2\pi/N_\phi$ , where  $N_\theta$  and  $N_\phi$  are the grid numbers. We set  $\Delta\theta = \Delta\phi$  by taking  $N_\phi = 2N_\theta$  (Table 1). The radial grid size  $\Delta r$  logarithmically increases with increasing  $r$  as

$$\Delta r(r) = r(10^f - 1), \quad (5)$$

where  $f \equiv \log(r_{\max}/r_{\min})/N_r$ ,  $N_r$  is the number of radial grid cells, and  $r_{\min}$  ( $r_{\max}$ ) is the radial inner (outer) boundary of the computational domain.

In order to avoid very short timesteps required for the dense gas near and within the star, we do not resolve the central structure. We instead assume a fixed central spherical sink cell of radius  $r_{\min}$ , within which a single star grows. The sink cell is assumed to be semi-permeable, meaning accretion flow into the sink is allowed, but there is no outflow. We evaluate mass accretion rates onto the star by measuring the gas inflow rates into the sink (also see Section 2.2). We set the sink radius  $r_{\min} = 30$  AU for our fiducial cases. Although the radius of an accreting protostar is generally much smaller than this sink size when  $\dot{M}_* \lesssim 10^{-2} M_\odot \text{ yr}^{-1}$  (e.g., Omukai & Palla 2003), an accreting star expands rapidly when  $\dot{M}_* \gtrsim 10^{-2} M_\odot \text{ yr}^{-1}$ , and inflates up to red supergiant radii. Hosokawa et al. (2012a) derive the mass-radius relationship for such a “supergiant protostar” accreting material above the critical rate,

$$R_*(M_*) \simeq 11.14 \text{ AU} \left( \frac{M_*}{100 M_\odot} \right)^{1/2}, \quad (6)$$

which is comparable to our sink cell size.

In the following, we will see that accreting protostars enter the supergiant stage for many of the examined cases. Even with the sink size  $r_{\min} = 30$  AU, our spherical coordinate system offers relatively high spatial resolution in the vicinity of the sink,  $(\Delta r \times r \Delta\theta)_{\min} \simeq 3.57 \text{ AU} \times 3.12 \text{ AU}$  for fiducial cases. This is even better than the finest resolution used in HS11  $\sim 10$  AU, so that the disk scale height is always resolved with several grid cells even in the innermost regions.

With this sink-cell technique, the gravitational potential  $\Phi$  has two components: one arising from the central

star  $\Phi_*$  and one from the gas' self-gravity  $\Phi_g$ ,

$$\Phi = \Phi_* + \Phi_g. \quad (7)$$

The specific gravitational force due to the central star is

$$-\nabla\Phi_* = -\frac{GM_*}{r^2}\mathbf{e}_r, \quad (8)$$

where  $\mathbf{e}_r$  is the radial unit vector. The potential for the gas' self-gravity  $\Phi_g$  is obtained by solving Poisson's equation

$$\Delta\Phi_g = 4\pi G\rho. \quad (9)$$

We make use of the Poisson solver developed in Kuiper et al. (2010a), which has been well tested and used with the PLUTO code.

### 2.1.2. Spatially Resolving the Jeans Length

Truelove et al. (1997) have suggested that, in order to avoid artificial fragmentation in numerical simulations, the Jeans length has to be spatially resolved by at least four cells. Recent studies argue that even higher resolutions are needed to correctly capture the gravity-driven turbulence that generally appears in the star formation process (e.g., Federrath et al. 2011; Turk et al. 2012; Meece et al. 2014), suggesting that the Jeans length should be resolved with 32-64 cells. Unfortunately, it is computationally prohibitive to consider the long-term ( $\sim 10^5$  years) evolution while fully satisfying this condition. We adopt the following ansatz instead:

For each cell and each timestep, we calculate the local Jeans length  $\lambda_J$  and monitor the ratio of  $\lambda_J$  to the greater of  $\Delta r$  and  $r\Delta\theta$ . When this ratio falls below a certain fixed number  $f_{\text{limit}}$ , we artificially squelch the cooling function in the energy equation, i.e.,

$$\Lambda \rightarrow 0 \quad \text{for} \quad \frac{\lambda_J}{\max(\Delta r, r\Delta\theta)} < f_{\text{limit}}. \quad (10)$$

We normally take  $f_{\text{limit}} = 12$  as our fiducial value. In practice, for a smooth transition, we evaluate the ratio  $\xi \equiv f_{\text{limit}} \max(\Delta r, r\Delta\theta)/\lambda_J$  and multiply the cooling rate by a suppressing factor when  $\xi$  exceeds unity,

$$C_{\text{limit}} = \exp\left[-\left(\frac{\xi - 1}{0.1}\right)^2\right], \quad (11)$$

which falls below  $10^{-4}$  for  $\xi \gtrsim 1.3$ .

With this procedure, the limit of radiative cooling varies across the grid due to differing spatial resolutions. Choosing a finer grid resolution  $\max(\Delta r, r\Delta\theta)$  overall means that the condition in equation (10) is satisfied for fewer cells and cooling operates without suppression for a larger number of cells. Because the disk becomes more unstable with more efficient cooling, disk fragmentation occurs more readily in simulations at higher grid resolution, which is also seen in other studies (e.g., Machida & Doi 2013). We study effects of varying the spatial resolution in Section 4.3 and show that, contrary to the predictions of previous studies, more fragmentation does not necessarily reduce the final stellar masses, but rather facilitates the formation of massive stars by inducing intermittent UV feedback more often.

### 2.1.3. Radiation Transfer

*Stellar UV radiation*— We consider different kinds of radiation which play different roles in our simulations. The stellar UV flux is the primary source of UV feedback which potentially halts the mass accretion onto stars and fixes the final stellar masses. We solve the transfer of ionizing (EUV) photons emitted by a protostar with a frequency-averaged approximation,

$$\frac{1}{r^2} \frac{\partial(r^2 F_{\text{EUV}})}{\partial r} = -n(1-x)\sigma_{\text{EUV}} F_{\text{EUV}}, \quad (12)$$

where  $F_{\text{EUV}}$  is the photon number flux above the Lyman limit,  $n$  the particle density,  $x$  the degree of ionization, and  $\sigma_{\text{EUV}}$  the photoionization cross section per particle, which is a function of the stellar effective temperature  $T_{\text{eff}}$ . Although the frequency-dependent UV transport can somewhat broaden primordial ionization fronts, which can enhance the thin-shell instabilities in the fronts (Whalen & Norman 2008), we do not expect that such an effect largely modifies the dynamics especially with dense media in the vicinity of the star. Equation (12) is easily integrated

$$F_{\text{EUV}} = \frac{S_{\text{EUV}}}{4\pi r^2} \exp(-\tau_{\text{EUV}}), \quad (13)$$

where  $S_{\text{EUV}}$  is the stellar EUV emissivity, and  $\tau_{\text{EUV}}$  the optical depth given by

$$\tau_{\text{EUV}} = \int_{r_{\text{min}}}^r n(1-x)\sigma_{\text{EUV}} dr' \quad (14)$$

(We implicitly assume no UV absorption within the sink cell).

We solve equations (13) and (14) making use of the adopted spherical grid (Section 2.1.1), i.e., along the radial cells having the same angular coordinate  $(\theta_j, \phi_k)$ . The obtained EUV flux  $F_{\text{EUV}}$  is used to provide the photoionization rate in the chemical rate equations and the associated heating rate in the energy equation. We consider the ionization of hydrogen only, treating helium as ‘‘hydrogenic’’, i.e., singly ionized within an HII region. For the purposes of our investigation, this approximation is not critical, but certainly could influence the precise numerical values of our results.

Within an HII region there is a component of diffuse EUV radiation emitted by the recombining gas, namely recombination of hydrogen directly into the ground state and recombinations of helium into the lowest states. HS11 have separately solved the transfer of diffuse hydrogen recombination photons using the flux-limited diffusion (FLD) approximation (Levermore & Pomraning 1981; Richling & Yorke 1997). However, UV feedback on the accreting material is mostly caused by the direct EUV stellar flux (also see Tanaka et al. 2013). Thus, we only solve for the transfer of the direct stellar EUV component and use the ‘‘on-the-spot’’ approximation (each recombination of hydrogen directly into the ground state causes the immediate ionization of a hydrogen atom in the vicinity). In praxis this is done by using a hydrogen recombination coefficient that excludes recombinations directly into the ground state.

As for the FUV radiation transfer, we only consider the stellar direct component, by exactly the same method using the self-shielding function (Draine & Bertoldi 1996)

as in HS11. We recognize that by excluding the diffuse components of EUV and FUV, one will encounter "shadowing" effects caused by UV-opaque clumps and the accretion disk itself. Our previous comparison studies with the 2D SE-RHD code have shown that this simplification does not significantly change the accretion history or final masses of the stars formed, which is the primary goal of this investigation.

*Molecular hydrogen line emission*— We follow the method used in HS11 for calculating the cooling rate via  $\text{H}_2$  line emission; we sum up the contributions from all "allowed" quadrupole transitions between the rotational and vibrational levels of  $J = 0 - 20$  and  $v = 0 - 2$ . To estimate the trapping effect for each transition, we approximate its optical depth  $\tau$  by the local Jeans length  $\lambda_J$ , i.e.,  $\tau = \alpha \lambda_J$ , where  $\alpha$  is the transition's absorption coefficient. This is a crude approximation compared to recently developed novel (and much more computationally expensive) methods (e.g., Clark et al. 2012; Hirano & Yoshida 2013; Greif 2014; Hartwig et al. 2015). In our current simulations, however, it is not reasonable to model the detailed thermal disk structure, because of our limitations in following the exact thermal state of the densest gas (Section 2.1.2). For a given spatial resolution, our treatment underestimates the cooling and thus leads to less gravitationally unstable disks. It therefore affects the quantitative behavior of disk fragmentation, such as the exact number and sizes of the emerging fragments. To assess the impact of the details of disk fragmentation on our final results, we vary our spatial resolution (see Section 4.3).

*Continuum emission*— As described in HS11, continuum cooling via  $\text{H}^-$  free-bound emission is important for the gas infalling onto the disk surface. HS11 have implemented this cooling process by solving continuum radiation transfer using the FLD approximation. In their 2D simulations, however, the  $\text{H}^-$  continuum emission is always optically thin throughout the evolution. This knowledge allows us to use a simpler approximation for the current 3D simulations; we simply subtract the  $\text{H}^-$  bounding energy 0.755 eV for each formation reaction  $\text{H} + e \rightarrow \text{H}^- + \gamma$  (R10 in Table 2) from the gas' internal energy. We have also implemented this method in our 2D SE-RHD code and confirmed the validity of this approximation.

We do not include the cooling via  $\text{H}_2$  collision-induced continuum emission (CIE, Omukai & Nishi 1998). This is because CIE only becomes important for the dense molecular gas with  $n \gtrsim 10^{13} \text{ cm}^{-3}$ , which only occasionally occurs in our simulations. Such dense gas normally lies close to the central star, primarily within the sink cell. Only with the enhanced spatial resolution considered in Section 4.3 below, however, does the density attain  $\sim 10^{14} \text{ cm}^{-3}$  in the densest parts of disks. Note that we do not pursue the exact thermal state of such tiny dense parts anyway, because of our inability to follow the long-term evolution at sufficiently high spatial resolution (see discussion in Section 2.1.2).

#### 2.1.4. Chemical Network for Primordial Gas

We have implemented an updated version of the primordial chemistry network used in HS11 and HR14 to the PLUTO code. Here, we solve for the non-equilibrium

Table 2. Chemical Reactions Included

No.	Reactions	References
R1	$\text{H} + e \rightarrow \text{H}^+ + 2 e$	1
R2	$\text{H}^+ + e \rightarrow \text{H} + \gamma$	2
R3 <sup>†</sup>	$\text{H}^- + \text{H} \rightarrow \text{H}_2 + e$	3
R4	$\text{H}_2 + \text{H}^+ \rightarrow \text{H}_2^+ + \text{H}$	4
R5	$\text{H}_2 + e \rightarrow 2 \text{H} + e$	4
R6 <sup>†</sup>	$\text{H}_2 + \text{H} \rightarrow 3 \text{H}$	5
R7 <sup>†</sup>	$3 \text{H} \rightarrow \text{H}_2 + \text{H}$	6
R8	$2 \text{H} + \text{H}_2 \rightarrow 2 \text{H}_2$	7
R9	$2 \text{H}_2 \rightarrow 2 \text{H} + \text{H}_2$	7
R10	$\text{H} + e \rightarrow \text{H}^- + \gamma$	4
R11	$\text{H} + \gamma \rightarrow \text{H}^+ + e$	2
R12	$\text{H}_2 + \gamma \rightarrow 2 \text{H}$	8, 9
R13	$2 \text{H} \rightarrow \text{H}^+ + e + \text{H}$	7
R14	$\text{H}^- + e \rightarrow \text{H} + 2 e$	1
R15	$\text{H}^- + \text{H}^+ \rightarrow 2 \text{H}$	4
R16*	$\text{H}^- + \text{H}^+ \rightarrow \text{H}_2^+ + e$	4
R17*	$\text{H}^- + \gamma \rightarrow \text{H} + e$	10
R18*	$\text{H} + \text{H}^+ \rightarrow \text{H}_2^+ + \gamma$	4
R19*	$\text{H}_2^+ + \text{H} \rightarrow \text{H}_2 + \text{H}^+$	4
R20*	$\text{H}_2^+ + e \rightarrow 2 \text{H}$	4
R21*	$\text{H}_2^+ + \text{H}^- \rightarrow \text{H}_2 + \text{H}$	11

<sup>†</sup> reaction rates updated with respect to HR14,

\* additional reactions added with respect to HR14

REFERENCES: (1) Abel et al. 1997, (2) Osterbrock & Ferland 2006, (3) Kreckel et al. 2010, (4) Galli & Palla 1998, (5) Martin et al. 1996, (6) Forrey 2013, (7) Palla et al. 1983, (8) Tielens & Hollenbach 1985, (9) Draine & Bertoldi 1996, (10) John 1988, (11) Millar 1991

chemical abundances of  $\text{H}$ ,  $\text{H}_2$ ,  $\text{H}^+$ ,  $e$ ,  $\text{H}^-$ , and  $\text{H}_2^+$  without the approximation of using the equilibrium value for  $\text{H}^-$  (as employed by e.g., Abel et al. 1997, HS11). The reactions included are summarized in Table 2.

As described in Section 3.1, HD molecules will form during the early collapse in some cases. The resulting HD molecular cooling reduces the temperature and density in the accretion envelope, which in turn leads to a somewhat slower initial protostellar growth (e.g., Yoshida et al. 2007, HS12). However, this effect ends during the early collapse by the time  $n \sim 10^8 \text{ cm}^{-3}$  and is unimportant thereafter. While we include deuterium chemistry for cosmological simulations following the early collapse stage (see Section 3.1 below), we do not in the current network for the accretion stage. We have checked with our previous 2D SE-RHD code with the same setting, starting after the density exceeds  $\sim 10^{10} \text{ cm}^{-3}$  as in HS12, that omitting the deuterium chemistry hardly changes the results.

#### 2.2. Stellar Evolution Calculations

We follow the evolution of the central protostar by solving the four stellar structure equations taking account of mass accretion (e.g., Stahler et al. 1980, 1986):

$$\left( \frac{\partial r}{\partial M} \right)_t = \frac{1}{4\pi\rho r^2}, \quad (15)$$

$$\left( \frac{\partial P}{\partial M} \right)_t = -\frac{GM}{4\pi r^4}, \quad (16)$$

$$\left( \frac{\partial L}{\partial M} \right)_t = \epsilon - T \left( \frac{\partial s}{\partial t} \right)_M, \quad (17)$$

$$\left(\frac{\partial s}{\partial M}\right)_t = \frac{GM}{4\pi r^4} \left(\frac{\partial s}{\partial p}\right)_T \left(\frac{L}{L_s} - 1\right) C, \quad (18)$$

where  $M$  is the Lagrangian mass coordinate,  $\epsilon$  the specific energy production rate by nuclear fusion,  $s$  the specific entropy, and  $L_s$  the radiative luminosity for an adiabatic temperature gradient. The coefficient  $C$  in equation (18) is given by the mixing-length theory for convective zones and is unity otherwise. Hydrogen burning via pp1-, pp2- and pp3-chains and via the CNO-cycle as well as helium burning via triple- $\alpha$  reactions are included.

In order to construct stellar models by solving the above equations, we adopt the numerical code **STELLAR**, originally developed by Yorke & Bodenheimer (2008), which uses the Henyey method. This differs from codes we used in HS11 and HR14, which employ shooting methods to solve the same equations (e.g., Omukai & Palla 2003; Hosokawa & Omukai 2009). We have confirmed that, despite a number of technical differences, both numerical codes provide essentially the same results for various different accretion histories (e.g., Hosokawa et al. 2010, 2013). Here, we adopt **STELLAR**, because the code offers relatively stable convergence properties for highly variable accretion rates. Kuiper & Yorke (2013) implemented **STELLAR** as their stellar evolution module in **PLUTO** to study present-day high-mass star formation assuming 2D axial symmetry. We make use of their implementation by suitably modifying the material functions (e.g., EOS, chemistry module, and opacity tables) for primordial star formation.

We start the stellar evolution calculations after the sink mass exceeds  $1 M_\odot$  via mass accretion, assuming an initial  $1 M_\odot$  polytropic star model obtained by solving the Lane-Emden equation with the index  $n = 1.5$ . A time sequence of stellar models are constructed as the stellar mass subsequently increases at the rate provided by the 3D RHD simulations. Varying the characteristics of the initial model (mass, radius, entropy, etc.) only affects the early evolution long before stellar UV feedback begins to operate (e.g., Hosokawa et al. 2010).

For the SE calculations, we use accretion rates averaged over a short duration: 300 years for the default cases and 30 years for cases with enhanced spatial resolution. This ‘‘smearing’’ of the instantaneous accretion rate measured at  $r = r_{\min}$  simulates the transport of material through the innermost part of the disk enclosed within the sink. Such a smearing and delaying timescale is given by the local viscous timescale, presumably several times longer than the Kepler orbital period,

$$P_{\text{Kepler}} \simeq 16.4 \text{ yr} \left(\frac{r}{30 \text{ AU}}\right)^{3/2} \left(\frac{M_*}{100 M_\odot}\right)^{-1/2}. \quad (19)$$

Note that accretion variability considered below occurs on much longer timescales than our assumed averaging timescale.

Mass accretion onto a protostar generally occurs through a circumstellar disk with finite angular momentum. Effects of disk accretion for the stellar evolution calculations can be modeled by considering proper outer boundary conditions (e.g., Palla & Stahler 1992). A simple way is adding the accreted gas to the stellar outermost zone with the same thermal state as in the atmosphere. This supposes an extreme ‘‘cold’’ disk accretion,

for which the gas lands on the stellar surface gently, having enough time to adjust its thermal state to that in the stellar atmosphere. The flow from the disk only covers a small part of the surface, and the other part freely radiates into a vacuum. In reality, however, the gas newly joining the star will carry some additional heat into the opaque interior. We approximate this ‘‘warm’’ accretion by allowing a fraction of the accretion luminosity to be advected into the star (e.g., Siess et al. 1997),

$$L_{*,\text{acc}} \equiv \eta L_{\text{acc}} = \eta \frac{GM_* \dot{M}_*}{R_*}, \quad (20)$$

where  $\eta$  is a parameter, which we normally set to  $\eta = 0.01$ . As shown in Hosokawa et al. (2013), however, the resulting stellar evolution is almost independent of varying  $\eta$ , except at early stages. Increasing  $\eta$  from 0 to 1 simply leads to earlier bloating of the star. Even for extreme ‘‘cold’’ disk accretion ( $\eta = 0$ ), bloating occurs long before radiative feedback becomes significant.

The stellar EUV and FUV emissivities are calculated assuming a black-body spectrum

$$S_{\text{EUV}} = 4\pi R_*^2 \int_{13.6 \text{ eV}}^{\infty} \frac{\pi B(T_{\text{eff}})}{h\nu} d\nu, \quad (21)$$

$$S_{\text{FUV}} = 4\pi R_*^2 \int_{11.2 \text{ eV}}^{13.6 \text{ eV}} \frac{\pi B(T_{\text{eff}})}{h\nu} d\nu, \quad (22)$$

(McKee & Tan 2008, HS11), where the effective temperature is given by

$$T_{\text{eff}} = \left(\frac{L_*}{4\pi R_*^2 \sigma}\right)^{1/4}, \quad (23)$$

where  $\sigma$  is Stefan-Boltzmann constant. We do not include the accretion luminosity  $(1 - \eta)L_{\text{acc}}$  (see equation 23), which presumably has spectral characteristics differing from a black-body at  $T_{\text{eff}}$ . This omission has little effect on our results, because the accretion luminosity  $L_{\text{acc}}$  is generally much smaller than the stellar luminosity  $L_*$  at the stage when UV feedback becomes effective. The contribution of the accretion luminosity may become large when the accretion rate suddenly rises as in a burst event. For these cases, however, the protostar also rapidly inflates for peak rates exceeding  $\sim 10^{-2} M_\odot \text{ yr}^{-1}$ . The stellar UV emissivity accordingly drops, which diminishes the UV feedback (also see Section 4.2.2 below). For accretion rate spikes below  $\sim 10^{-2} M_\odot \text{ yr}^{-1}$ , the accretion luminosity does not significantly affect the total luminosity.

### 3. CASES CONSIDERED

#### 3.1. Primordial Cloud Collapse in Cosmological Simulations

We study the formation of primordial stars in a full cosmological context. To this end, we first follow the formation and gravitational collapse of a number of primordial clouds utilizing a modified version of 3D SPH/N-body code **GADGET-2** (e.g., Springel 2005; Yoshida et al. 2006; Hirano & Yoshida 2013). The procedures for this step are well described in our previous investigations HR14 and HR15, who in total have investigated the evolution of more than 1600 clouds in a standard  $\Lambda$ CDM

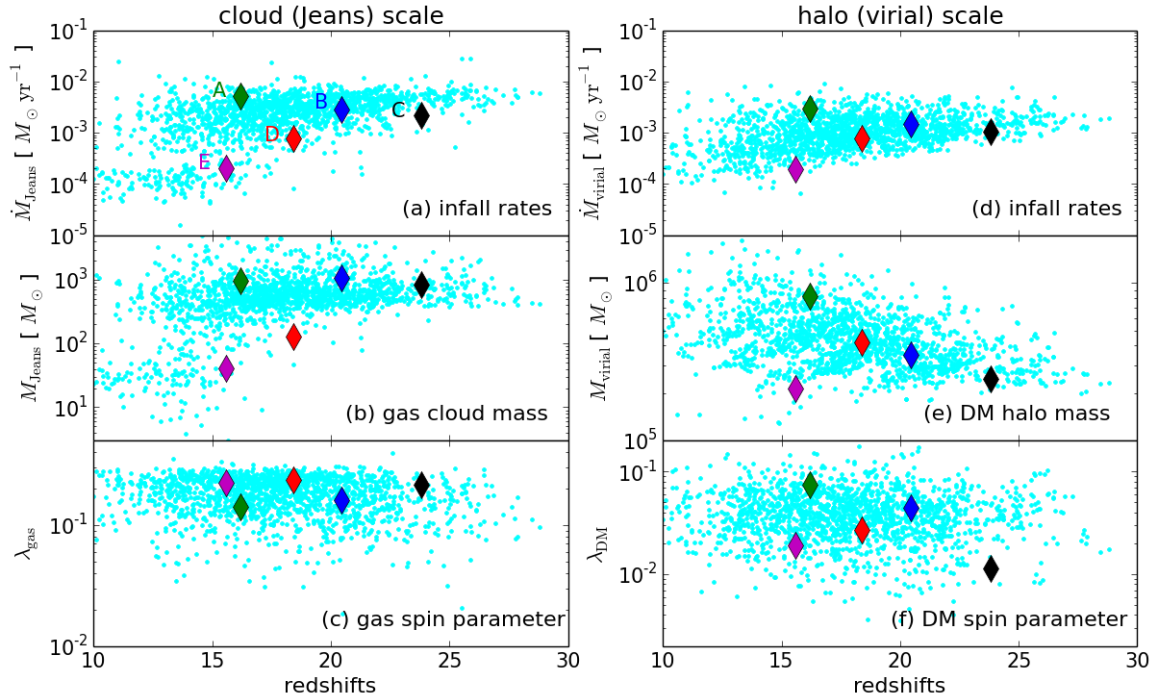


FIG. 1.— Physical properties of the cosmological cases considered here (colored rhombuses denoting cases A–E; see also Table 1) compared to the cosmological samples analyzed in Hirano et al. (2015) (cyan dots). *Left column*: physical properties of gas clouds measured at the self-gravitating cloud (Jeans) scale, (a) infall rates, (b) masses, and (c) spin parameters as a function of the formation redshifts. *Right column*: same as the left column but for the dark matter halo (virial) scale. The masses and spin parameters presented in (e) and (f) are only for the DM components.

universe. The hierarchical zoom-in and particle-splitting techniques have been used to follow the cloud evolution with sufficiently high spatial resolution in cosmological volumes.

We focus on five representative cases A–E taken from the cosmological samples of HR14 and HR15. For each case, we followed the run-away collapse until the central density reaches  $\simeq 10^{13-14} \text{ cm}^{-3}$  (HR14). Here, we study the subsequent evolution in 3D, using the method described in Section 2. For initial conditions, we remap the particle-based cosmological simulation data onto our 3D spherical grid. The coordinate origin is set at the density maximum and we allow a single star to grow within the assumed sink, normally  $r < 30 \text{ AU}$ . The direction of the polar axis is taken to be that of the angular momentum vector for the gas enclosed in the inner region  $r \leq 0.01 - 0.1 \text{ pc}$ . With this choice, the circumstellar disk that is formed is nearly perpendicular to the polar axis (but see discussion on fluctuations of the disk’s orientation in Section 4.2.2). Table 1 summarizes several important parameters defining the examined cases. In addition to the default cases A–E, we also consider additional cases identified by suffixes for a number of different parameter settings and/or different grid resolutions.

HR14 have previously studied the evolution of the same cases with 2D SE-RHD simulations, modifying the initial conditions to fit their axisymmetric grid configuration. Table 1 summarizes their final stellar masses attained after UV feedback halted the mass accretion. HR14 demonstrate that the final stellar masses tend to be somewhat higher for higher accretion rates aver-

aged over  $\sim 10^5$  years after the formation of the protostars. Since accretion histories are predestinated by the envelope structure set in the early collapse stage, higher stellar masses result from a higher global infall rate  $\langle 4\pi r^2 \rho v_r \rangle$  during the collapse, where  $v_r$  is the radial component of the velocity. In particular, a good estimator of the final stellar mass can be constructed using the infall rate  $\dot{M}_J$  measured at the self-gravitating cloud (Jeans) scale, defined as the radius  $r_J$  where the ratio of the enclosed gas mass  $M_{\text{enc}}(r)$  to the the local Bonner-Ebert mass  $M_{\text{BE}}$  reaches its maximum as a function of radius  $r$ , i.e.,  $M_{\text{enc}}(r_J)/M_{\text{BE}} = \max(M_{\text{enc}}(r)/M_{\text{BE}})$ . HR15 have derived a fitting formula relating the final stellar masses and cloud-scale infall rates,

$$M_* = 250 M_{\odot} \left( \frac{\dot{M}_J}{2.8 \times 10^{-3} M_{\odot} \text{ yr}^{-1}} \right)^{0.8}, \quad (24)$$

where the infall rates are measured when the cloud central density reaches  $10^7 \text{ cm}^{-3}$ . Figure 1 shows the diversity of the cloud-scale infall rates and relevant quantities: the masses and spin parameters at the cloud (Jeans) and halo (virial) scales. We see that the five cases A–E considered here well cover the distribution of  $\sim 1500$  cases studied in HR15.

The cloud-scale infall rates for cases A–E decrease in alphabetical order, as do the final stellar masses obtained in the 2D SE-RHD simulations (see Table 1). HR15 show that, despite such diversity, the distribution of stellar masses evaluated for the  $\sim 1500$  cases has a pronounced peak at  $M_* \simeq 250 M_{\odot}$ . This suggests the presence of

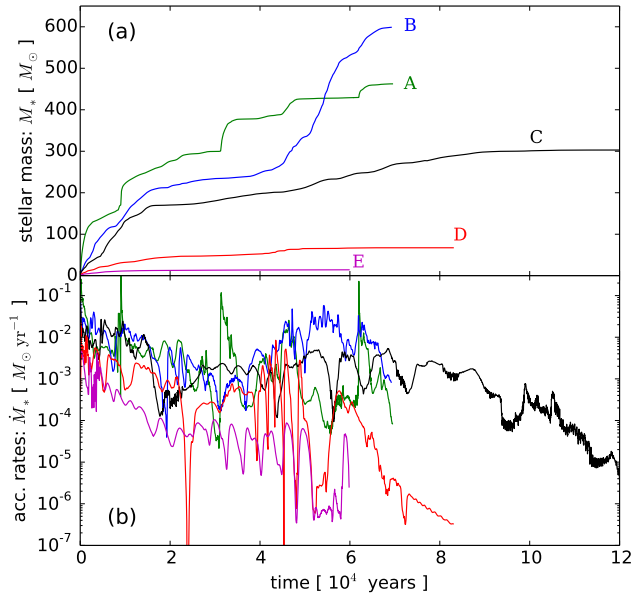


FIG. 2.— Time evolution of the stellar masses (panel a) and accretion rates (panel b) for cases A (green), B (blue), C (black), D (red), and E (magenta). The time  $t = 0$  corresponds to the formation of embryo protostars.

a fiducial initial condition for primordial star formation. Among our five cases, cases A–C are more representative of such a fiducial condition than cases D and E.

Case E provides the lowest final stellar mass  $M_* \simeq 24.4 M_\odot$  in 2D. For this case, HD line cooling also operates in addition to  $H_2$  cooling in the collapse stage. The temperature consequently drops to a few  $\times 10$  K, limited by the cosmic microwave background floor. HR14 show that the HD-cooling mode can be triggered when the collapse is somewhat slower than for purely spherical free-fall. Such a slow collapse can occur, for example, when rotational support decelerates the collapse. In the protostellar accretion stage, UV feedback typically limits the stellar masses to a few tens of  $M_\odot$  (e.g., HS12; HR14).

We assume that the primordial clouds for cases A–E do not experience any external feedback. In reality, however, FUV radiation from nearby stars can alter the thermal evolution during collapse and consequently the resulting final stellar masses (e.g., Oh & Haiman 2002; O’Shea & Norman 2008). HR15 show that, by considering the spatial distribution of FUV fields created by Pop III stars at different redshifts, these so-called Pop III.2 stars (e.g., Bromm et al. 2009; O’Shea et al. 2008) become comparable in number to the so-called Pop III.1 primordial stars, for which the external feedback is negligible. Interestingly, HR15 show that the final stellar masses and cloud-scale infall rates still have the same correlation among the different sub-populations of III.1 and III.2 stars. We examine how this correlation can differ in 3D, focusing on the interplay between variable mass accretion and UV radiative feedback.

In addition to the cosmological cases described above, we perform simulations starting with idealized initial conditions: a homogeneous, zero-metallicity gas cloud in solid body rotation with constant density, temperature, and chemical composition. The results of these idealized

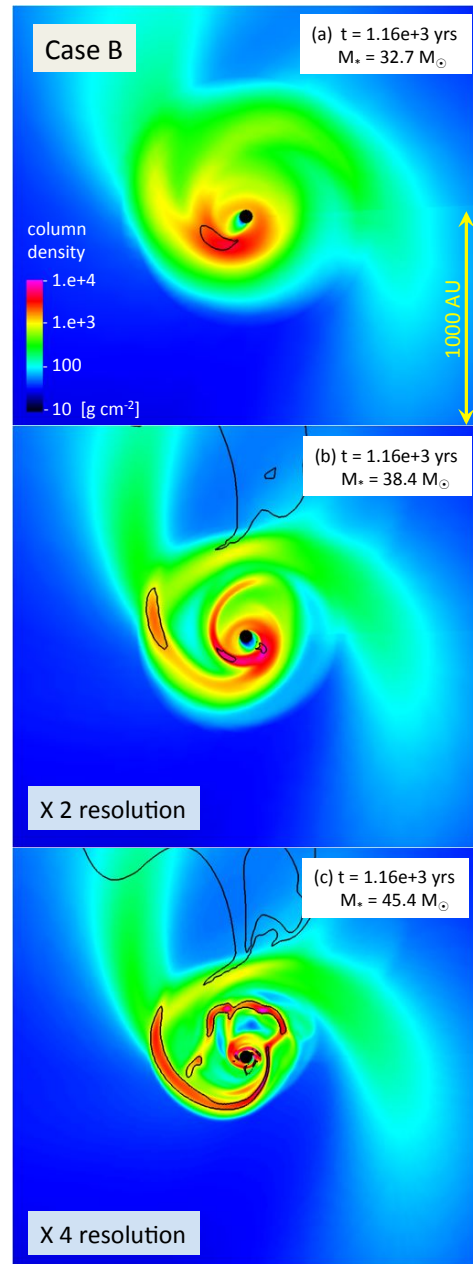


FIG. 3.— Gas column density along the polar direction of the self-gravitating circumstellar disks obtained with different spatial resolution (cases B-NF, B-NF-HR2-m0, B-NF-HR4-m20 for panels a, b, and c, respectively; see text and Table 1). The snapshots are shown at the same epoch  $t = 1.16 \times 10^3$  years, but the accreted stellar masses differ due to different prior accretion histories. In each panel, the black contours mark the positions where the Toomre- $Q$  parameter takes the value of  $Q = 0.3$ .

simulations are discussed in the Appendix. These more simplified initial conditions allow us to test the effects of varying numerical settings in a controlled manner.

## 4. RESULTS

### 4.1. Overall Results

We first summarize the simulation results for our fiducial cases A–E. As seen in Figure 2-(a), the stellar mass



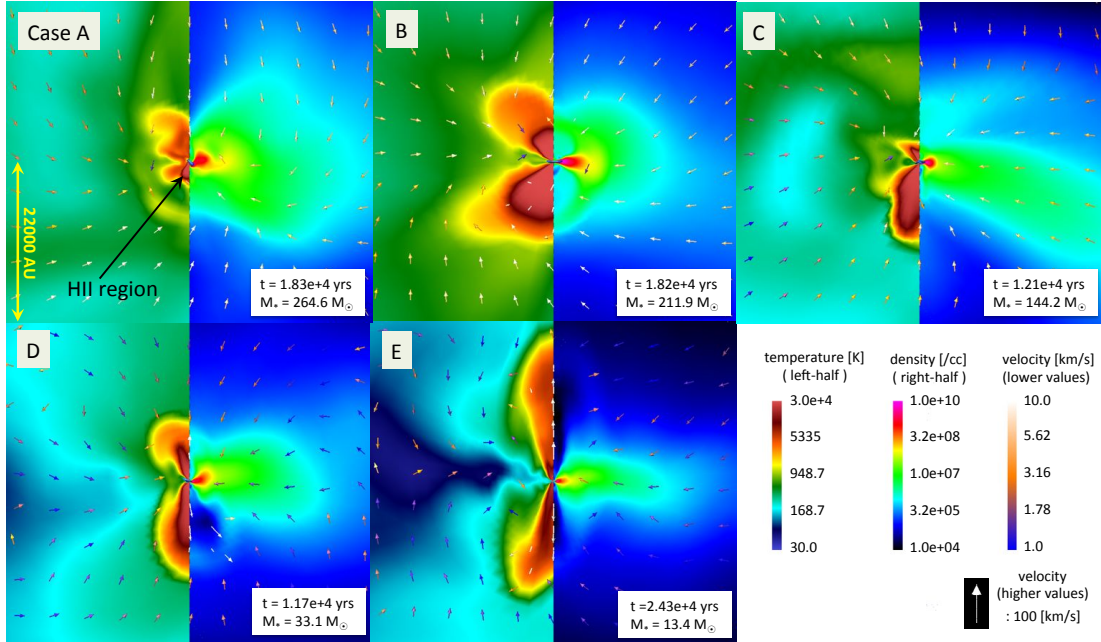


FIG. 4.— Temperature, density, and velocity structure of cases A–E in a plane containing the polar axis at the time when the polar extension of HII regions first reaches  $10^4$  AU. In each panel, the gas temperature is shown to the left and the density distribution to the right. Velocity vectors  $v < 10 \text{ km s}^{-1}$  are depicted by small blue and orange arrows, whereby the color gradation represents the magnitude. Velocities  $v > 10 \text{ km s}^{-1}$  are depicted by white arrows with lengths varying in proportion to the magnitude (see the legend in the lower-right panel). The small 3D magenta contour at the panel center delineates the iso-density surface for  $10^{10} \text{ cm}^{-3}$ , which roughly traces an accretion disk around the central star. Each panel also shows the elapsed time and stellar mass.

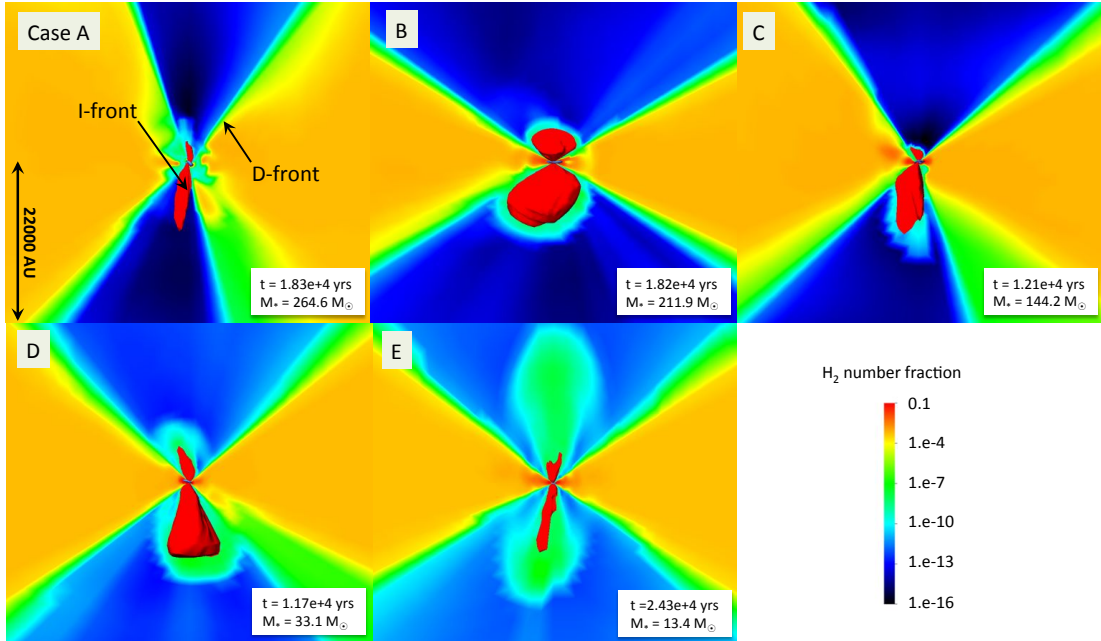


FIG. 5.— Same as Figure 4 but for the chemical structure in the accretion envelope. In each panel, the color image shows the distribution of the hydrogen molecular number fraction in the same vertical plane as in Figure 4. The 3D red contour delineates the structure of ionization fronts, within which the hydrogen atomic fractions is below 0.5.

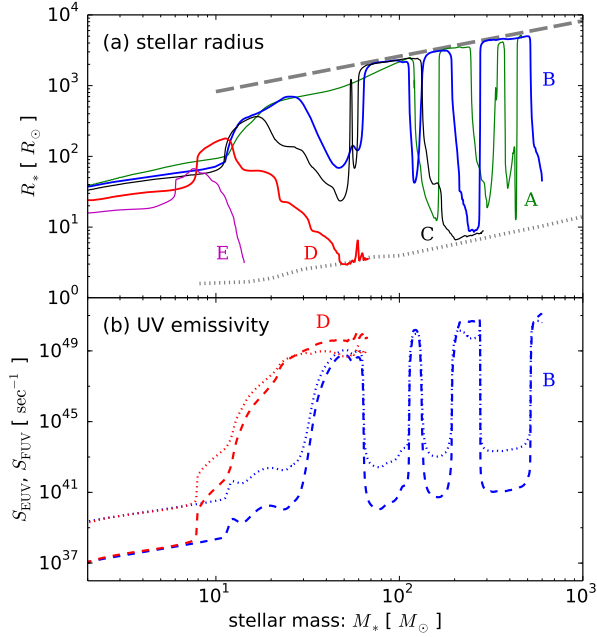


FIG. 6.— Evolution of the stellar radius (panel a) and UV emissivities (panel b) as a function of accumulated stellar mass. The different colors represent the same cases as in Figure 2. In panel (a), the thick gray dotted and long-dashed lines represent the mass-radius relationships for zero-age main-sequence stars and for supergiant protostars (equation 6). In panel (b), the dashed line represents the stellar ionizing (EUV;  $h\nu \geq 13.6$  eV) flux and the dotted line the dissociating (FUV;  $11.2$  eV  $\leq h\nu \leq 13.6$  eV) radiation. For clarity, we only show the UV emissivities for the two representative cases B and D.

growth histories show a great variety in the  $\sim 10^5$  years after the formation of embryo protostars. Ordinary massive stars with  $M_* < 100 M_\odot$  result in cases D and E. In particular, the final stellar mass is only  $\sim 15 M_\odot$  for case E. For cases A–C, on the other hand, the stellar masses reach several hundred solar masses at the end of the simulations.

Figure 2-(b) displays the highly variable accretion histories for all cases. Such a high degree of variability is a well-known feature of mass and angular momentum transport through self-gravitating circumstellar disks. Figure 3 presents examples of the density structure of self-gravitating disks seen in our simulations. The disk has non-axisymmetric spiral arms, which produce the gravitational torques leading to variable mass accretion. In Figure 2-(b), we see that the mass accretion finally ceases for cases C–E; the mean accretion rates for the last  $10^4$  years having fallen down to  $\sim 10^{-5} M_\odot \text{ yr}^{-1}$  due to UV feedback. For cases A and B, however, the accretion rates are still higher than  $10^{-4} M_\odot \text{ yr}^{-1}$  at  $t = 7 \times 10^4$  years. Although the simulations end at this point due to high computational costs, the stellar masses will continue to increase via accretion, because UV feedback has not yet become fully effective.

Figures 4 and 5 shows that, for all cases, bipolar HII regions form and grow within the larger  $\text{H}_2$  photodissociation regions (PDRs) within a few  $\times 10^4$  years after stellar birth. Although the snapshots look quite similar, the stellar masses at the evolutionary stage of HII region formation differ significantly among the cases; the stellar mass is lower in alphabetical order for cases A through

E. For cases A–C, it is not until the stellar masses exceed  $100 M_\odot$  that the HII regions appear. For cases D and E, however, only a few  $\times 10 M_\odot$  stars can create HII regions.

The diversity of stellar masses which first form an HII region comes from the different protostellar evolution with different accretion histories (Fig. 6). For cases D and E, the protostar contracts from its bloated state when  $M_* \gtrsim 10 M_\odot$ ; this is the so-called Kelvin-Helmholtz (KH) contraction phase (e.g., Omukai & Palla 2003). The stellar UV emissivities dramatically increase during this stage as the effective temperature rises as  $T_{\text{eff}} \propto R_*^{-1/2}$ . Stellar contraction continues until the star arrives at the zero-age main-sequence (ZAMS). As a result, the HII region emerges for  $M_* \simeq 10 M_\odot$ . For cases B and C, however, KH contraction is interrupted by the abrupt stellar expansion occurring around  $M_* \simeq 50 M_\odot$ . For case A, there is no contraction stage until the stellar mass exceeds  $100 M_\odot$ . It is only after the stellar mass reaches a few hundred solar masses that the protostar substantially contracts. Since the stellar UV emissivity sensitively depends on the effective temperature, the epoch of stellar contraction actually controls when the HII region first appears.

For cases A–C, the protostar enters the supergiant stage with rapid mass accretion  $\dot{M}_* \gtrsim 0.01 M_\odot \text{ yr}^{-1}$  before KH contraction begins (Section 2). Several studies presuppose that supergiant protostars only appear in extreme cases of primordial star formation, for which very high accretion rates are available (e.g., direct-collapse model, see Bromm & Loeb 2003). However, HR14 and HR15 show with 2D SE-RHD simulations that the supergiant stage can appear even for more typical Pop III.1 cases when accretion rates are relatively high but not necessarily extremely high. By contrast, our 3D SE-RHD simulations now demonstrate that the supergiant stage is a common feature of primordial star formation. This is due to the highly variable mass accretion onto primordial protostars caused by self-gravitating disks, for which the accretion rates temporarily and recurrently exceed the critical rate for expansion to the supergiant stage. As a result of such variable mass accretion, in fact, stellar contraction and re-expansion are repeated several times for cases A and B. The volatile evolution of the stellar radius results in strong fluctuations of the stellar UV emissivity. This variability causes recurrent extinction and re-formation of HII regions (see Section 4.2.2 below). UV feedback only intermittently operates and cannot efficiently stop mass accretion. Very massive stars can potentially form by this mechanism.

Although our results are resolution dependent because of the ansatz explained in Section 2.1.2, the basic features described become more prominent at higher spatial resolution (Section 4.3). This is demonstrated in Figure 3, showing that higher resolution results in sharper and finer density substructure within the disk. The resulting mass accretion is more variable with increased spatial resolution, bringing the central protostar to the supergiant stage more often. Disk fragmentation (e.g., Fig. 3-c) does not necessarily reduce the final stellar masses. The emerging fragments cause repeated accretion bursts when falling onto the star, which can extinguish the stellar UV emission and thus ultimately enhances stellar

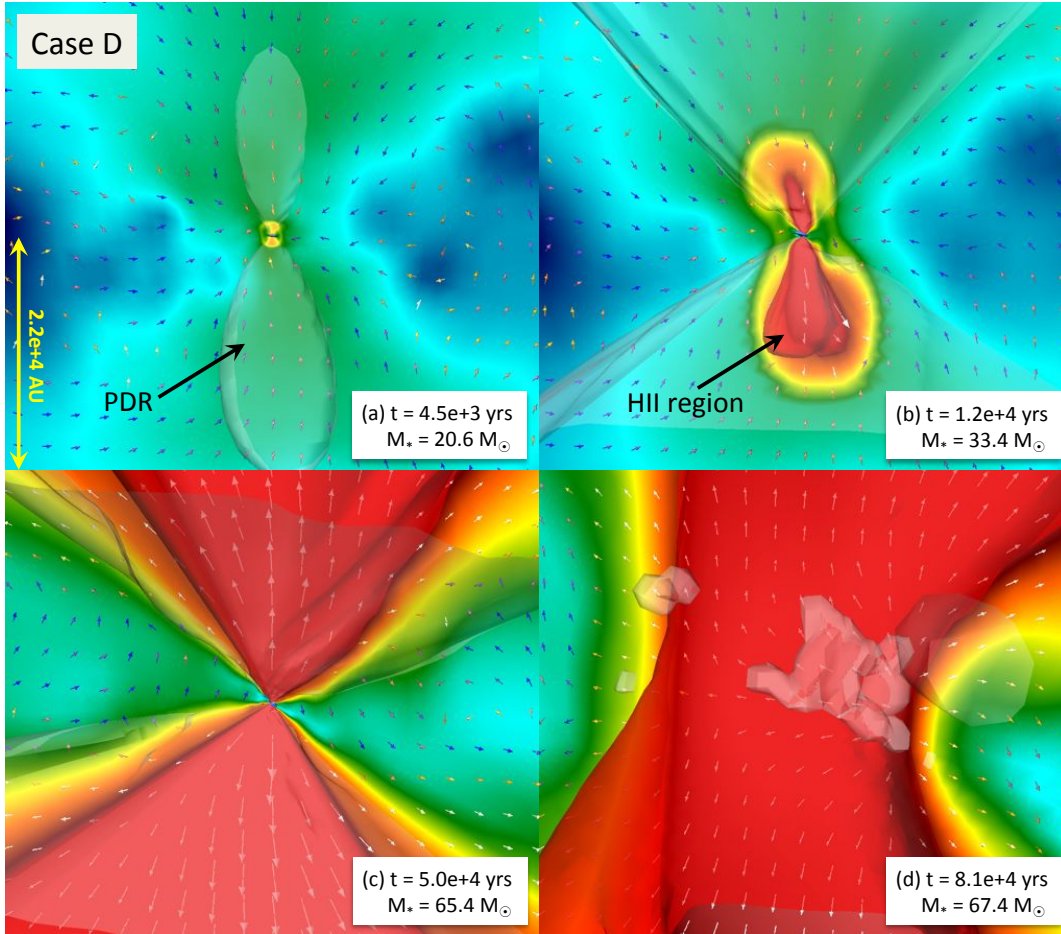


FIG. 7.— Time evolution of the temperature distribution in a plane containing the polar axis for case D. The stellar mass and evolutionary time are given in the insets of panels (a)–(d). The color scale for temperature is the same as in Figure 4. The 3D white and red contours delineate the structure of dissociation and ionization fronts, within which the hydrogen atomic and molecular fractions are below  $0.5$  and  $10^{-4}$ , respectively.

mass growth.

#### 4.2. Mass Accretion under the Stellar UV Feedback

##### 4.2.1. Massive Stars with Tens of Solar Masses: UV Feedback Halts the Mass Accretion

We first describe in detail the evolution of cases D and E, which produced ordinary massive stars with tens of solar masses. As shown below, the evolution for these cases is similar to that found in our previous 2D SE-RHD simulations (HS11; HS12).

*Case D*— Figure 7 presents the evolution of the temperature structure for case D as an  $H_2$  PDR and an HII region expand into the accretion envelope. After the protostar enters the KH contraction stage (see Fig. 6), the stellar FUV emissivity rises and forms a bipolar  $H_2$  PDR (Fig. 7-a). At the same time, the stellar EUV emissivity increases and slightly later creates a bipolar HII region within the larger PDR (Fig. 7-b). The PDR and HII region continue to grow and expand as shown for the epoch  $t = 5 \times 10^4$  years (Fig. 7-c), but these regions are still centrally “pinched” because a circumstellar disk blocks the stellar UV radiation close to the disk plane.

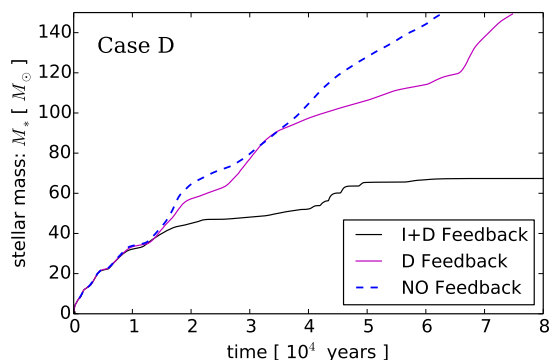


FIG. 8.— Example of the impact of differing stellar UV feedback on stellar mass growth. The black solid (case D), magenta solid (case D-DF), and blue dashed lines (case D-NF) represent the cases including both the ionizing and dissociating feedback, with the dissociating feedback only, and without UV feedback, respectively.

However, even the gas protected from the UV photons is disturbed by shocks that propagate into the envelope ahead of the ionization fronts. Comparing Figure 7-(b) and (c), we see that even the gas outside the PDR is

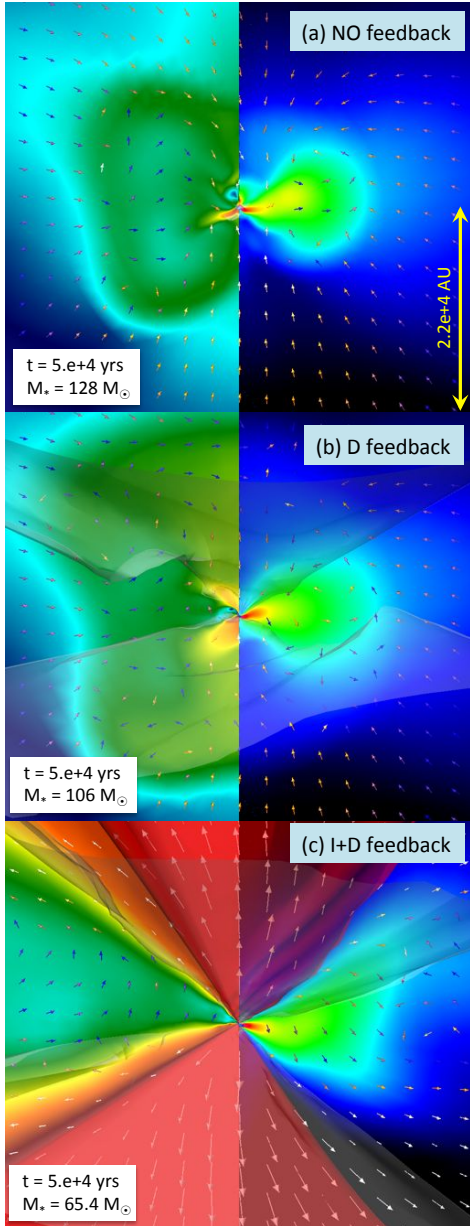


FIG. 9.— Impact of differing stellar UV feedback on the accretion envelope: (a) no feedback (case D-NF), (b) only photo-dissociating feedback (case D-DF), and (c) both photo-ionizing and dissociating feedback (case D). The temperature, density and velocity distributions are shown at the same epochs,  $5 \times 10^4$  years after the birth of the central protostar. Note that the stellar masses differ among the cases because of the different mass accretion histories (also see Fig. 8). The illustration is in the same style as in Figure 4.

heated up by shock compression. HS11 have shown that the mass influx from the envelope onto the disk is hindered by this effect. Moreover, the disk loses mass via photoevaporation, being exposed to the stellar EUV radiation. The HII region is filled by the photoevaporating outflow launched from the disk surface. Ultimately, the circumstellar disk is destroyed due to photoevaporation, allowing the HII region to expand in equatorial directions (Fig. 7-d), and accretion onto the star is effectively shut

off for  $M_* \simeq 67.4 M_\odot$  at  $t = 8 \times 10^4$  years.

In Figure 8, we plot the evolution of the stellar mass for case D (solid black line). For comparison, we show the stellar mass growth for case D-NF (blue dashed line), for which all UV feedback effects had been turned off. We see that mass accretion onto the protostar is significantly reduced by UV feedback effects. This figure also displays the stellar mass growth for a test case (case D-DF) that only included photodissociation (FUV) feedback (solid magenta line). Comparing these mass growth histories we conclude that FUV feedback does hinder mass accretion somewhat, but its impact is much weaker than EUV feedback.

Figure 9 shows the variation of the envelope temperature - density - velocity structure with differing UV feedback effects. For case D-NF with neither EUV nor FUV feedback (Fig. 9-a), the disk is surrounded by a warm ( $T \simeq 300 - 500$  K) envelope, where compressional heating due to gas infall is balanced by  $H_2$  molecular line cooling. The gas temperature is higher ( $T \simeq 5000$  K) in a central region  $r \lesssim 10^3$  AU, where  $H^-$  free-bound emission is the main cooling process. For case D-DF with only FUV feedback (Fig. 9-b), the warm envelope is larger, because FUV radiation reduces the abundances of efficient coolants via  $H_2$  photodissociation and  $H^-$  photodetachment. However, this only occurs in polar regions. Because the bulk of stellar FUV radiation is blocked by the disk, the envelope structure is hardly affected in equatorial directions, where the disk mostly accretes gas from the envelope. As seen in Fig. 9-c EUV feedback dramatically changes the envelope structure. In addition to the bipolar photoevaporation flow within the HII region, portions of the envelope outside the HII region are expelled from the computational grid as shocks propagate through the envelope and spread the pressure excess of ionized gas.

Our results demonstrate that FUV feedback does reduce mass accretion rates, which qualitatively agrees with 3D RHD simulations performed by Susa (2013). However, the FUV feedback seen in our simulations seems to be weaker than in Susa (2013), who claims that FUV feedback is largely responsible for terminating mass accretion onto primordial protostars. We discuss possible causes of this difference in Section 4.2.3 below.

*Case E*— The evolution of case E is qualitatively similar to that for case D, except that HD molecular line emission also contributes to the cooling in the early collapse stage. During collapse, in general, the thermal evolution of the central homogeneous core strongly affects the radial structure of the accretion envelope. Since the radius of the core is well approximated by the Jeans length, the envelope temperature and density at a given radius  $r$  obey  $r = \lambda_J \propto T^{1/2} \rho^{-1/2}$ , i.e., a lower temperature implies a lower density. In case E the accretion envelope thus has relatively low temperatures and densities, which can be seen in Figure 4. KH contraction begins at lower stellar masses with correspondingly lower accretion rates (Fig. 6). The final stellar mass is also lower than for case D,  $M_* \simeq 14.3 M_\odot$ .

#### 4.2.2. Massive Stars with Hundreds of Solar Masses: Intermittent UV Feedback with Variable Mass Accretion

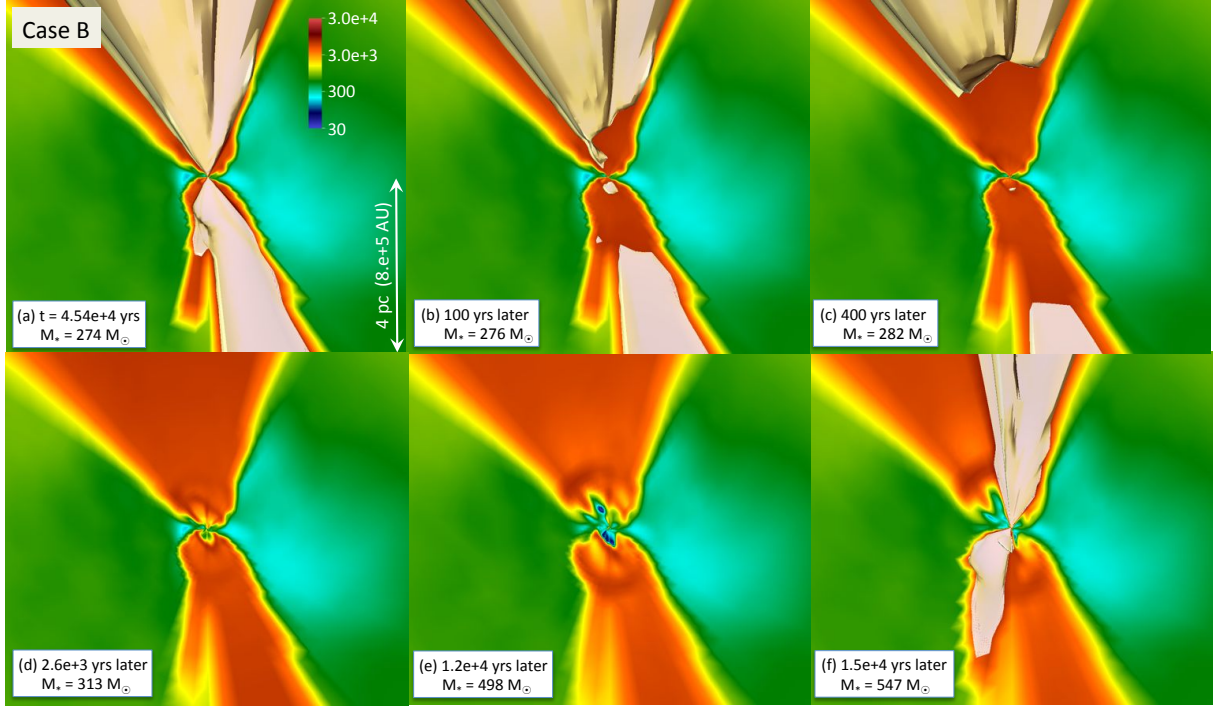


FIG. 10.— The extinction and re-formation of HII regions for case B. In each panel, the 3D yellow contour delineates the structure of the ionization front (as in Figures 5 and 7 with the red contours), and the color image shows a 2D slice of the temperature distribution (color scale as in Figure 4). The panels (a)–(f) show a time sequence for  $t > 4.54 \times 10^4$  years after the birth of the protostar; the elapsed time after the epoch of panel (a) is given for (b)–(f). Note that the box size is more than 50 times larger than in Figure 7.

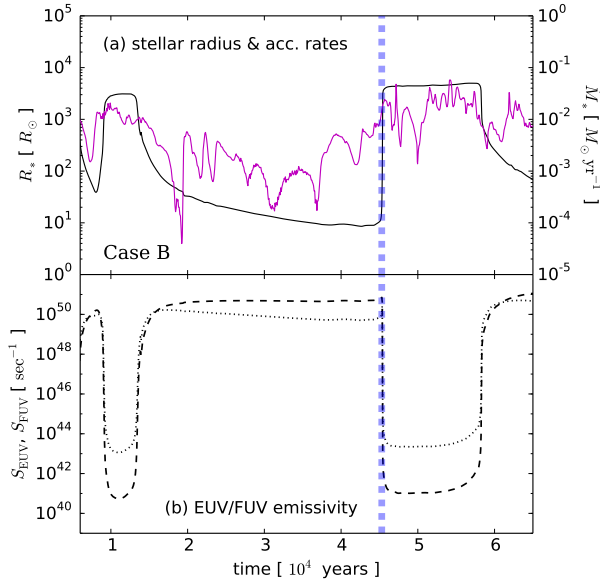


FIG. 11.— Effects of the variable mass accretion on the evolution of the stellar radius (panel a) and UV emissivities (panel b) for case B. In panel (a), the black and magenta lines show the time evolution of the stellar radius and accretion rates respectively. In panel (b), the dashed and dotted lines represent the stellar EUV and FUV emissivities as in Figure 6-(b). The vertical blue dotted line marks the epoch of the stellar inflation at  $t = 4.53 \times 10^4$  years (also see Fig. 12).

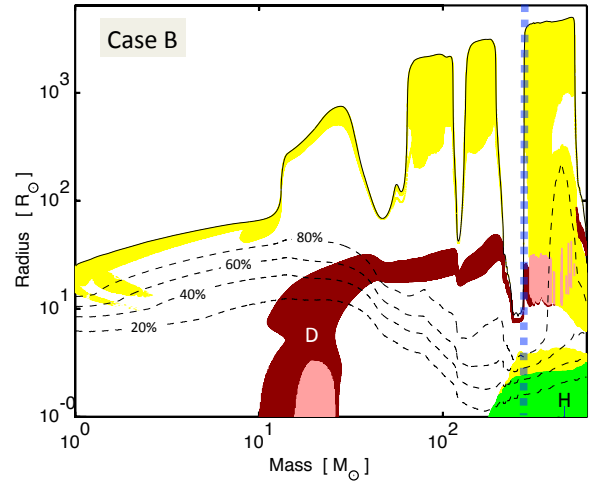


FIG. 12.— Evolution of the stellar interior structure as a function of increasing mass for case B. The black solid and dashed lines represent the radial positions of the photosphere and mass coordinates 80%, 60%, 40%, and 20% of the total stellar mass. The yellow regions denote convective zones and white regions radiative zones, each without active nuclear burning. The pink and brown stripes denote convective and radiative deuterium-burning zones, respectively and green depicts the central convective hydrogen-burning zone. Layers with active nuclear burning are indicated if the depletion time of the “burning” species is shorter than the lifetime of a main-sequence star with the equivalent mass. The vertical blue dotted line marks the same epoch as indicated in Figure 11.

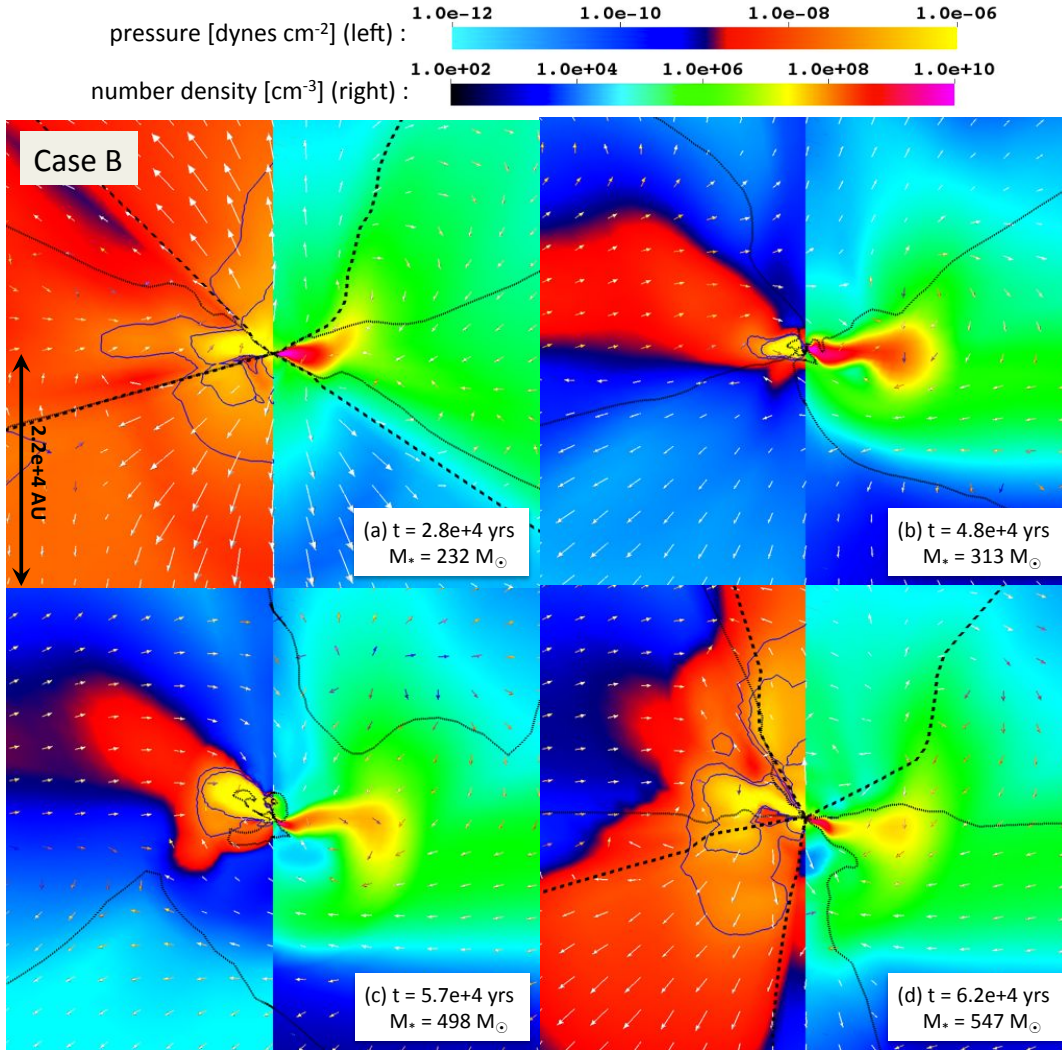


FIG. 13.— The evolution of pressure (left-half of each panel) and density (right-half) under the influence of intermittent UV feedback for case B. Panels (b)–(d) show the same epochs as in Figure 10 (d)–(f) but on a smaller physical scale. The 2D velocity vectors are presented in the same style as in Figure 4. In each panel, the short dashed line delineates the location of the hydrogen ionization front and the solid gray line depicts the dissociation front, whereby the fractional atomic and molecular abundances are 0.5 and  $10^{-4}$ , respectively. The thin blue lines in the left panels show the pressure contours for  $P = 1$  and  $0.3 \times 10^{-7}$  dynes  $\text{cm}^{-2}$ .

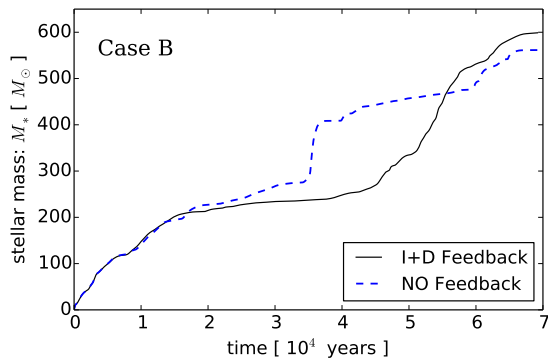


FIG. 14.— Same as Figure 8 but for case B, i.e., the black solid and blue dashed lines represent the evolution for cases B and B-NF.

Next we describe the results for cases A–C, for which very massive ( $M_* \gtrsim 250 M_\odot$ ) stars form that pass through a supergiant evolutionary stage.

*Case B*— Figures 10 and 11 show that for case B, variable mass accretion leads to abrupt and radical changes of the stellar radius and the associated recurrent extinction and re-formation of HII regions. A bipolar HII region, which have formed prior to  $t \simeq 4.5 \times 10^4$  years (Fig. 10-a), begins to retreat in a direction away from the star a few hundred years later (Fig. 10-b,c), shortly after the accretion rates rise above  $\sim 10^{-2} M_\odot \text{yr}^{-1}$  and the protostar rapidly inflated to a supergiant (Fig. 11-a). Due to the protostar’s expansion the stellar EUV emissivity accordingly drops by almost ten orders of magnitude (Fig. 11-b), initiating the extinction of the HII region.

Figure 12 depicts the evolution of the stellar interior structure for this case B. Although the star initially begins KH contraction when  $M_* \simeq 30 M_\odot$ , the contraction is interrupted by a phase of rapid accretion at  $M_* \simeq 45 M_\odot$ . The star quickly and substantially bloats up again, because the accretion rate exceeds

$\sim 10^{-2} M_{\odot} \text{ yr}^{-1}$ , and only begins to contract after the accretion rate falls during a subsequent quiescent phase (also see Fig. 11-a). The abrupt expansion depicted in detail in Figures 10 and 11 occurs for  $M_* \simeq 274 M_{\odot}$ ; it is the third of such events. Figure 12 shows that, even during the supergiant stage, an inner core with a large fraction of the total mass continues to contract while releasing gravitational energy. Only a surface layer with a tiny fraction of the stellar mass participates in the bloating up, trapping a part of the energy transferred from the contracting core. We note that hydrogen burning occurs in the stellar center for  $M_* \gtrsim 180 M_{\odot}$  and conclude that rapid mass accretion will even trigger the bloating of an H-burning star and extinguish its stellar UV emissivity.

The HII region begins to recombine each time it loses its exciting UV source. Because the recombination timescale varies as  $t_{\text{rec}} \propto 1/n_{\text{HII}}$ , hydrogen recombination occurs in the densest region first. Within the bipolar HII region, the radial density gradient is established by the photoevaporation flow with geometrical dilution, which roughly follows

$$n_{\text{HII}} \sim 10^4 \text{ cm}^{-3} \times \left( \frac{r}{10^4 \text{ AU}} \right)^{-2} \left( \frac{v_{\text{evp}}}{100 \text{ km sec}^{-1}} \right)^{-1} \left( \frac{\dot{M}_{\text{evp}}}{10^{-3} M_{\odot} \text{ yr}^{-1}} \right), \quad (25)$$

where  $\dot{M}_{\text{evp}}$  and  $v_{\text{evp}}$  are the photoevaporation rate and flow velocity, normalized with typical values (e.g., Hollenbach et al. 1994; Tanaka et al. 2013). The structure of recombining ionized gas thus resembles a “recombination front”, starting at the dense inner regions and propagating outward through the bipolar HII region (Fig. 10-b,c). The recombination timescale for the current case is

$$t_{\text{rec}} \sim 100 \text{ years} \left( \frac{n_{\text{HII}}}{10^4 \text{ cm}^{-3}} \right)^{-1}, \quad (26)$$

which matches the fast propagation of the recombination front shown in Figure 10-(b-c).

Even after the ionized gas has recombined, the hot atomic gas still remains as a “remnant” of the HII region (or fossil HII region) for a long time (Fig. 10-c,d). This recombined atomic gas still flows outward through inertia, but it is no longer replenished via photoevaporation of the disk. The temperature of the expanding recombined atomic gas gradually decreases due to adiabatic cooling and Ly- $\alpha$  cooling. About  $1.2 \times 10^4$  years after the extinction of the UV source (Fig. 10-d), for instance, the remnant neutral gas has  $\simeq 1000 - 5000$  K over  $\sim$ pc scales. The central regions  $r \lesssim 10^5$  AU have the coldest ( $T \lesssim 100$  K) gas because of strong adiabatic cooling.

Whereas the signature of a fossil HII region remains over  $\sim$ pc scales for many thousands of years, influences of the stellar UV radiation in the stellar vicinity  $r \lesssim 10^4$  AU disappear much quicker. Figure 13-(a) shows that the pressure structure of the accretion envelope is greatly modified by a bipolar HII region if present. The radial pressure gradient created by the photoevaporation outflow spreads over the envelope even beyond the HII region (also see Section 4.2.1). However, after the stellar UV emissivity shuts off, these pressure structures quickly disappear. At the epoch depicted in Figure 13-(c), almost no signatures of UV feedback are present. The

$M_* \simeq 500 M_{\odot}$  protostar quiescently accretes the gas through the circumstellar disk with negligible stellar radiative feedback.

Figure 14 shows the stellar mass growth history for this case. We see that UV feedback does hinder the mass accretion for  $2 \lesssim (t/10^4 \text{ years}) \lesssim 4.5$ , when a bipolar HII region emerges (also see Figs. 11 and 13-a). However, the accretion flow is no longer halted once the HII region disappears at  $t \simeq 4 \times 10^4$  years. The gas accumulated in the envelope thus far begins to fall back toward the star. As a result, the stellar mass rapidly increases during the period  $4.5 \lesssim (t/10^4 \text{ years}) \lesssim 6$ , during which the protostar remains in the supergiant stage emitting few ionizing photons.

After the star has accreted most of the gas accumulated in the envelope, the accretion rate gradually decreases for  $t \gtrsim 6 \times 10^4$  years. The protostar then begins to contract, and the stellar UV emissivity dramatically increases again (Fig. 11). Figure 10-(f) shows that a bipolar HII region begins to grow again within the hot ( $T \simeq 5000$  K) atomic envelope, the remnant of the previous HII region that disappeared after the star had inflated. Figure 13-(d) shows that the photoevaporation outflow refills the HII region. The pressure structure of the accretion envelope is accordingly modified by the expanding HII region. At this point UV feedback begins to regulate the mass accretion as before.

For this case B, however, UV feedback only intermittently operates during the  $7 \times 10^4$  years considered, so that the stellar mass growth is not efficiently reduced. Figure 14 shows that, in fact, UV feedback only temporarily postpones stellar mass growth. At the end of the simulation, the stellar mass is slightly higher than for the comparison case B-NF,<sup>1</sup> for which UV feedback has been turned off. This slightly accelerated stellar mass growth can be understood as follows. As described above, the gas accumulated in the envelope outside the disk rapidly falls back toward the star-disk system once the HII region disappears for  $t \gtrsim 4 \times 10^4$  years. With the resulting rapid mass supply from the envelope, the disk becomes highly gravitationally unstable. This promotes the gravitational torque operating in the disk, which consequently helps the stellar mass growth.

*Case A:*— Intermittent UV feedback is also seen in case A. Figure 15 shows that variable accretion causes the abrupt expansion of the stellar radius and rapid drop of UV emissivities as in case B. This case exemplifies a characteristic feature of stellar evolution with accretion bursts. For instance, let us focus on the short accretion burst of duration  $\sim 10^2$  years occurring at  $t \simeq 10^4$  years. The high rate of accretion for this burst causes the protostar to inflate, terminating KH contraction. The protostar remains swollen in the supergiant stage for  $\sim 10^4$  years, long after the accretion rate had dipped below

<sup>1</sup> For case B-NF, there is a big jump of the stellar mass at  $t \simeq 3.5 \times 10^4$  years. Although we do not resolve those additional individual infalling clumps that would appear at higher resolution (see Figure 3), variable accretion is a general feature even at the default resolution. Interestingly, the inner part of the B-NF disk is greatly tilted at  $t \simeq 3.5 \times 10^4$  years. It is known that external tidal perturbations from the surrounding non-axisymmetric envelope could excite the “bending wave”, which enhances the disk inclination and angular momentum transport (e.g., Papaloizou & Terquem 1995).

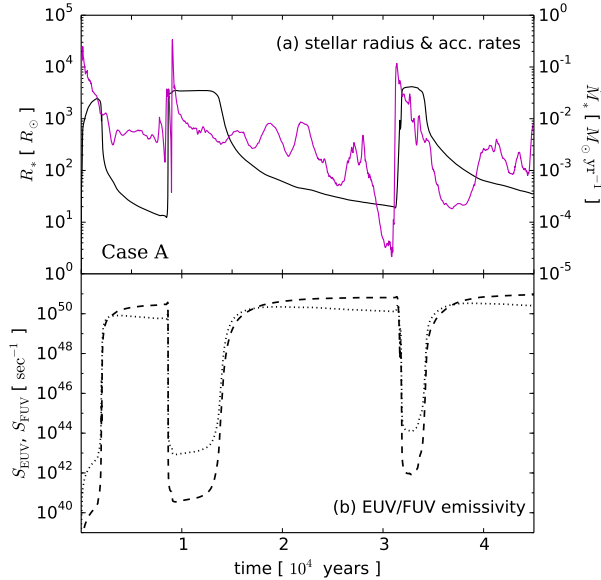


FIG. 15.— Same as Figure 11 but for case A.

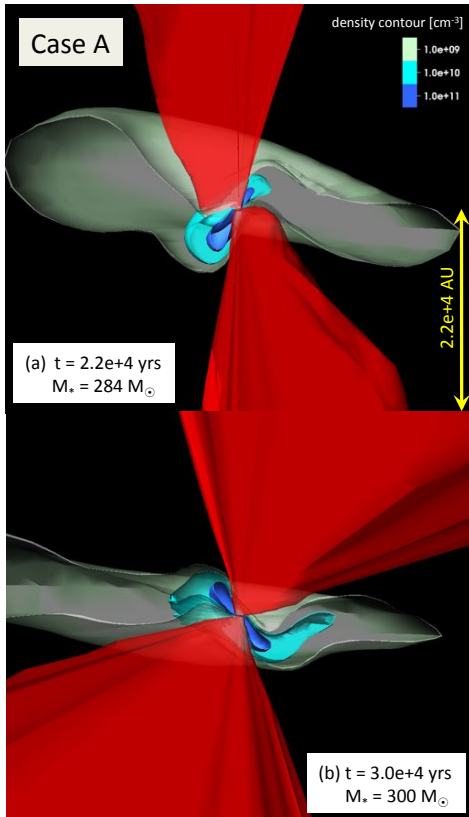


FIG. 16.— Example of a precessing accretion disk with a bipolar HII region as seen for case A. The panels (a) and (b) depict the density and ionization structure as viewed from the same angle for the evolutionary times  $2.2 \times 10^4$  years and  $3 \times 10^4$  years after the birth of the protostar. The dark blue, cyan, and green-gray contours represent cut-outs of the iso-density surfaces for  $n_{\text{H}} = 10^{11}$ ,  $10^{10}$ , and  $10^9 \text{ cm}^{-3}$ , respectively. The red contours delineate the HII region.

$\dot{M}_* \lesssim 10^{-2} M_{\odot} \text{ yr}^{-1}$ . This is because, whereas the protostar can react almost immediately to a high accretion rate and quickly expands, it can contract only on a KH timescale even if the accretion drops to zero (e.g., Sakurai et al. 2015). Thus, even short episodes of accretion bursts can have a long-lasting impact on the star’s evolution. A similar feature is also seen for the second burst event at  $t \simeq 3 \times 10^4$  years. This effect can only be correctly simulated by solving for the stellar interior structure simultaneously with time-dependent accretion histories, as provided by SE-RHD simulations.

In our simulations, circumstellar disks normally form perpendicular to the polar axis of the spherical coordinate system because of our choice of the polar axis orientation (see Section 3.1). The orientation of the disk occasionally fluctuates with time, however, especially for cases A and B, for which the spin parameters measured at the cloud scale are relatively low (Fig. 1). For instance, Figure 16 shows the density contours of the disk and ionization contours of the bipolar HII region at different epochs for case A. Although viewing from the same angle, the orientations of the HII region as well as the disk changes with time. Since the primordial cloud forms through cosmological structure formation and is not necessarily perfectly axisymmetric, material falling onto the disk has different mean angular momentum vectors at different times. Similar phenomena have been also reported for present-day star formation, whereby turbulent motions in molecular clouds easily twist the distribution of the angular momentum (e.g., Bate et al. 2010; Fielding et al. 2015). Due to this disk “precession”, the stellar EUV radiation can ionize the envelope gas over rather wide opening angles. The orientation of the disk at any particular time also depends on whether or not UV feedback is included in the simulations. This is not surprising because UV feedback blows away the gas in the polar regions and modifies the pressure structure even near the equator. As a result, UV feedback can modify the accretion history of both angular momentum and mass from the envelope onto the disk.

*Case C:*— For our case C, which also shows the intermittent UV feedback in an early stage, we follow the much longer evolution than the above. For cases A and B, mass accretion is still on-going under intermittent UV feedback for  $7 \times 10^4$  years, because episodes of rapid mass accretion are able to interrupt the KH contraction sufficiently often. Although it is uncertain how long this evolution can continue for these cases, UV feedback will likely fix the final stellar masses, if KH contraction remains uninterrupted for a sufficiently long time. Our case C exemplifies this evolution. After the protostar enters the supergiant stage for  $M_* \gtrsim 50 M_{\odot}$ , the star again begins KH contraction, after the stellar mass reaches  $\sim 130 M_{\odot}$  at  $t \simeq 10^4$  years (Fig. 6). The bipolar HII region quickly expands as the star approaches the ZAMS. Mass accretion is not immediately shut off by UV feedback, however, but continues at a much reduced rate. As a result, the star’s mass almost doubles by  $t \simeq 1.2 \times 10^5$  years, when the accretion rate falls below  $10^{-5} M_{\odot} \text{ yr}^{-1}$ .

#### 4.2.3. Comparison to 2D SE-RHD Results

As mentioned in Section 3.1, HR14 have previously studied the evolution of protostellar accretion for the



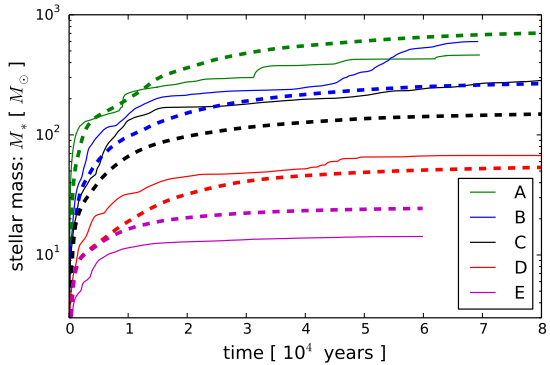


FIG. 17.— Stellar mass growth histories obtained in the current 3D SE-RHD simulations compared to our previous 2D results (Hirano et al. 2014). The solid lines represent the 3D cases with the same colors as in Figure 2-(a); dashed lines depict the 2D results for the same clouds.

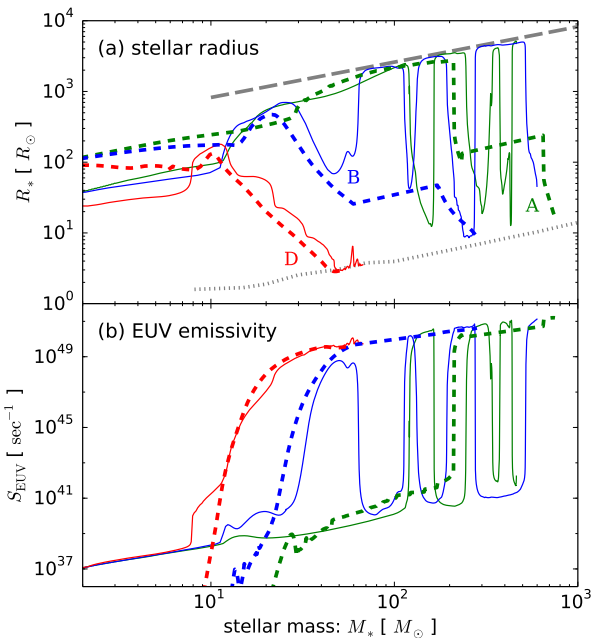


FIG. 18.— The protostellar evolution of radius and UV emissivities for the 3D cases considered here in comparison to those of our previous 2D calculations (Hirano et al. 2014). This illustration is almost the same as Figure 6; the panels (a) and (b) show the evolution of the stellar radius and EUV emissivity with increasing mass. For clarity only cases A, B, and D are presented. The thick dashed lines represent the 2D results for the same clouds as in Figure 17.

same primordial clouds considered above, but under the assumption of 2D axial symmetry. Figure 17 presents the stellar mass growth histories for both the current 3D and the previous HR14 2D results in comparison. We see that the 3D results roughly match the overall trends of the 2D results, in spite of a number of technical differences between the adopted numerical codes. Comparing the 2D and 3D results for each case, the stellar masses at a given epoch differ by a factor of a few at most. Some differences come from the fact that, for a 2D simulation, the original 3D structure of a natal cloud is modified to fit the 2D axisymmetric grid by averaging physical quantities over the azimuthal direction. Moreover, the 2D

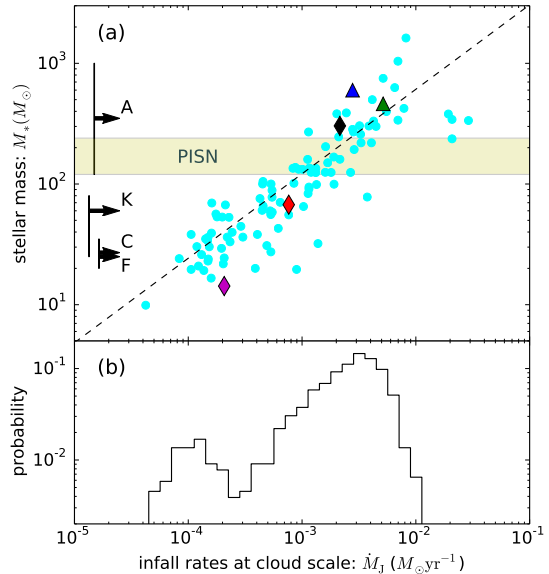


FIG. 19.— *Panel (a)*: correlation between the final stellar masses and infall rates measured at the cloud (Jeans) scale when the cloud central density is  $\simeq 10^7 \text{ cm}^{-3}$ . The rhombuses and triangles denote the current 3D results for cases A (green), B (blue), C (black), D (red), and E (magenta). The triangles are lower limits to the mass, indicating that mass accretion continues beyond  $t = 7 \times 10^4$  years, the end of the simulations. The cyan dots represent the 2D SE-RHD results for about 110 cosmological cases studied by Hirano et al. (2014). The dashed line represents the fitting formula for these 110 cases given by equation 24. The horizontal yellow bar denotes the expected mass range of progenitors of pair-instability supernovae,  $120 M_\odot \lesssim M_* \lesssim 240 M_\odot$  (Yoon et al. 2012). The arrows mark the estimated stellar masses of Pop III supernova progenitors, which have been estimated from the abundance patterns of recently-discovered Galactic metal deficit stars: (A) SDSS J001820.5-093939.2 (Aoki et al. 2014), (K) SMSS J031300.36-670839.3 (Keller et al. 2014), (C) SDSS J102915+172927 (Caffau et al. 2011), and (F) SD 1313-0019 (Frebel et al. 2015). The vertical bar associated with each arrow represents the possible mass range discussed in the literature (e.g., Schneider et al. 2012; Ishigaki et al. 2014). *Panel (b)*: probability distribution of the cloud-scale infall rates in the 1540 cosmological cases studied by Hirano et al. (2015) (also see their Fig. 17).

results also depend on the somewhat ad-hoc use of an  $\alpha$ -viscosity to model the gravitational torque operating in self-gravitating disks.

Figure 18 shows the protostellar mass and UV emissivities as a function of stellar mass for several representative cases. For case D, the evolution is quite similar between 3D and 2D cases. The qualitative differences appear for cases A and B, where both the stellar radius and EUV emissivity abruptly change for  $M_\odot \gtrsim 100 M_\odot$  because of the variable accretion encountered in 3D (also see Section 4.2.2). In our previous 2D cases, by contrast, there was an intermediate stage between the supergiant and ZAMS stage, where the stellar radius gradually increases with the mass (named the “P2” path in HR14). Stellar evolution calculations demonstrate that this behavior is generally present, when the accretion rates are in the range of  $4 \times 10^{-3} M_\odot \text{ yr}^{-1} \lesssim \dot{M}_* \lesssim 10^{-2} M_\odot \text{ yr}^{-1}$  (e.g., Omukai & Palla 2003). For 2D cases, this stage appears because the accretion rates smoothly evolved with time. In 3D, however, the highly variable accretion rates do not remain in this narrow range very long. The intermediate P2 stage thus does not occur in our 3D cases.

Instead, the protostar evolves back and forth between the supergiant and ZAMS stages depending on details of the variable accretion history. This effect reduces the stellar EUV emissivity for  $M_* \gtrsim 100 M_\odot$  in comparison with the 2D cases, as episodes of rapid accretion bring the star back to the supergiant stage several times.

Figure 19-(a) displays the stellar masses at the end of the 3D simulations as a function of the infall rates measured at the cloud (Jeans) scale (see Section 3.1), demonstrating that the 3D results still show a similar correlation as found in 2D. Considering the fact that the masses for cases A and B are only lower limits, the correlation found in 3D appears to have a steeper slope than for the 2D results (equation 24), albeit with much poorer statistical significance (five cases in 3D). This does not necessarily agree with Susa et al. (2014), who do not find this correlation in their 3D RHD simulations. We discuss this issue in Section 5.2 separately.

As Figure 19-(b) shows, primordial clouds taken for cases A–C offer rather typical initial conditions for primordial star formation. Our results suggest that the very massive stars, even above the mass range of the pair-instability supernovae (PISN) progenitors  $120 M_\odot \lesssim M_* \lesssim 240 M_\odot$  (Yoon et al. 2012), can form for such typical cases. A significant number of  $\sim 10^3 M_\odot$  BHs might be produced as remnants of these very massive primordial stars. We shall discuss possible observational signatures of such massive primordial stars in Section 5.4.

### 4.3. Varying Spatial Resolution

#### 4.3.1. Disk Fragmentation and Accretion Bursts

Although our 3D simulations show a new 3D effect of the intermittent UV feedback, the ansatz described in Section 2.1.2 can bring some resolution-dependence which can affect the evolution quantitatively. It is thus necessary to explore how resolution affects the results of our simulations. First, we shall focus on case B described in Section 4.2.2, for which UV feedback becomes important when the stellar mass exceeds  $200 M_\odot$  at  $t \gtrsim 2 \times 10^4$  years (Fig. 14). For this case, we study effects of increasing the grid resolution during early times before UV feedback begins to operate.

We first recalculate the evolution of case B with our standard resolution, turning off UV feedback (case B-NF; see Table 1). We use four model configurations of case B-NF at different epochs for  $M_* \simeq 0, 40, 70,$  and  $120 M_\odot$  as the starting configurations for calculations at higher spatial resolution. Next, we interpolate each of the four starting model configurations onto a grid with double the resolution for each spatial coordinate and follow the evolution for 3000 years. These test cases are named as B-NF-HR2-mX, where the suffix “mX” represents the restarting point at  $M_* \simeq X M_\odot$  (see Table 1). The duration of 3000 years is comparable to the Kepler orbital period  $P_{\text{Kepler}} \simeq 1600$  yr for typical values of stellar mass  $M_* \simeq 50 M_\odot$  and disk radius  $\sim 500$  AU (c.f. equation 19). The accretion envelope surrounding the disk typically has a density  $\lesssim 10^9 \text{ cm}^{-3}$ , for which the free-fall timescale is  $\gtrsim 3 \times 10^3$  years. Mass infall from the envelope onto the disk at the higher resolution hardly affects the evolution, whereas cooling, fragmentation, and the associated mass and angular momentum transport within the disk occur on much shorter timescales and

therefore should be affected by varying spatial resolution.

Figure 20 compares the stellar mass growth and accretion histories for the examined cases. We see that mass accretion becomes more strongly variable with higher resolution; i.e., the accretion rates vary over shorter timescales and with much higher variations:  $10^{-4} M_\odot \text{ yr}^{-1} \lesssim \dot{M}_* \lesssim 0.1 M_\odot \text{ yr}^{-1}$  (Fig. 20-b). Furthermore, the mass that the star accretes during the  $3 \times 10^3$  years is somewhat larger with higher resolution, independent of the different starting points of the doubly-resolved cases (Fig. 20-a). This can be understood with the help of Figure 3, which displays the face-on disk structure at  $t \simeq 1.2 \times 10^3$  years for the different resolutions. The disk clearly has sharper and finer density structure at higher resolution. This is because radiative cooling is less restricted by our ansatz and the disk is thus more gravitationally unstable. Since gravitational torques are caused by the non-axisymmetric disk structure such as spiral arms, increasing the resolution can lead to more efficient mass and angular momentum transport through the disk, which results in a higher stellar mass.

We once again double the resolution using case B-NF-HR2-m0 at  $t \simeq 600$  years as a starting model, a time at which  $M_* \simeq 20 M_\odot$ , and recalculate the evolution (case B-NF-HR4-m20). We repeat these higher resolution simulations with a larger cooling limit  $f_{\text{limit}} = 24$  (case B-NF-HR4-m20-fc; see Section 2.1.2) and a larger sink cell radius  $r_{\text{min}} = 52$  AU (case B-NF-HR4-m20-lsk). The resolution is now 4 times higher than the original case B-NF. Because of the high computational cost, the highest resolution simulations are evolved for only  $10^3$  years. Figure 21 compares the stellar mass growth and accretion histories of these quadruple resolution cases with the results of the lower resolution simulations. The resolution dependences discussed above appear again more prominently.

Case B-NF-HR4-m20’s accretion history displays lots of spiky features, representing multiple accretion burst events (Fig. 21-b). The stellar mass growth over  $10^3$  years is correspondingly greater at higher resolution (Fig. 21-a). Figures 3-(c) and 22 show that, at this high resolution, one of the spiral arm breaks up and creates two fragments. These and Figure 23-(a) show the distributions of the Toomre  $Q$ -parameter on the equator, defined by

$$Q = \frac{c_s \Omega}{\pi G \Sigma}, \quad (27)$$

where  $c_s$  is the local sound speed and  $\Sigma$  is the vertical column density. Because the spiral arms have  $Q \lesssim 1$ , gravitational instability makes them prone to fragmentation. This feature is not seen at lower resolution for the same epoch (Fig. 3-a, b). The evolution for this case is quite similar to that shown in Vorobyov et al. (2013), who study disk fragmentation using 2D face-on (thin disk) simulations at even higher resolution than ours.

Our results suggest that the stellar mass growth is not hindered, but rather accelerated due to disk fragmentation. This is because newly created fragments rapidly migrate inward through the disk and ultimately accrete onto the star. This behavior is shown in Figure 22, tracking the orbital motion of the fragments seen in Figure 3-

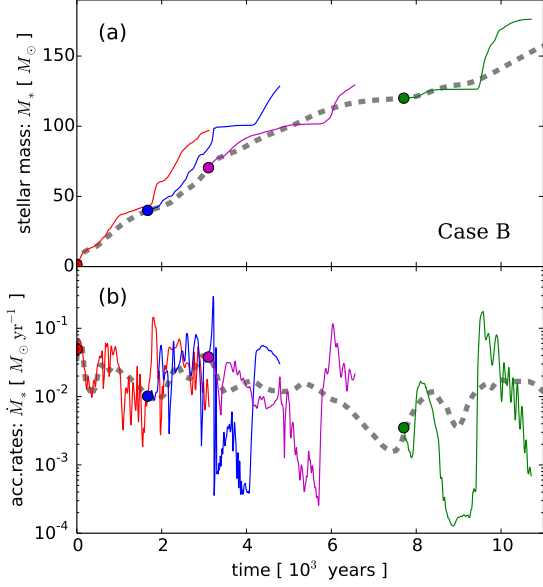


FIG. 20.— Comparison of the mass growth histories with different spatial resolutions in halo B cases. The panels (a) and (b) show the time evolution of the stellar masses and accretion rates onto the protostar. In both panels, the thick dashed lines represent case B-NF. The solid lines represent the cases with 2 times higher spatial resolution: B-NF-HR2-m0 (red), B-NF-HR2-m40 (blue), B-NF-HR2-m70 (magenta), and B-NF-HR2-m120 (green). The filled circles mark the starting points of these doubled-resolution cases, i.e., when the stellar mass is  $\simeq 1 M_\odot$ ,  $40 M_\odot$ ,  $70 M_\odot$ , and  $120 M_\odot$  for case B-NF (also see text).

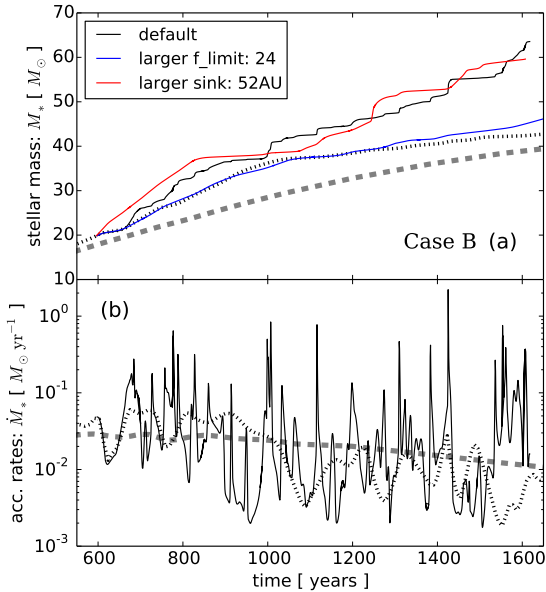


FIG. 21.— Same as Figure 20 but including cases at 4 times higher spatial resolution than case B-NF (thick dashed lines) and 2 times higher resolution than case B-NF-HR2-m0 (dotted lines). The solid lines represent cases (see text and Table 1) B-NF-HR4-m20 (black), B-NF-HR4-m20-fc (blue), and B-NF-HR4-m20-lsk (red). In panel (b), accretion histories for cases B-NF, B-NF-HR2-m0, and B-NF-HR4-m20 only are shown for clarity.

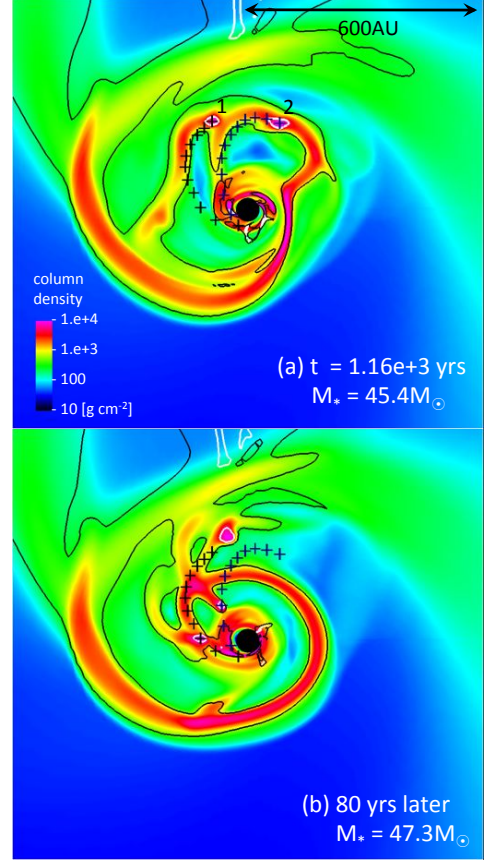


FIG. 22.— Inward migration of two fragments (crosses) for case B-NF-HR4-m20. As in Figure 3, colors represent the gas column density but for a smaller region around the central star. The black (white) contours delineate the boundaries where the Toomre- $Q$  parameter takes the value  $Q = 1.0$  ( $Q = 0.1$ ). Spiral arms and fragments consistently have  $Q < 1$ . *Panel (a)*: Evolutionary age  $t = 1.16 \times 10^3$  years (the same moment as in Fig. 3) *Panel (b)*: 80 years later. The black and dark-blue crosses mark the positions of the two fragments every 10 years.

(c). Both fragments rapidly migrate inward and reach the star in less than 100 years. Recent 3D simulations by Greif et al. (2012) also report a similar rapid migration in highly gravitationally unstable disks. Greif et al. (2012) conclude that the typical timescale for such migrations is roughly the local free-fall timescale, the shortest timescale for any physical process driven by gravity. For our case B-NF-HR4-m20, the density near the disk mid-plane is  $n \gtrsim 10^{11} \text{ cm}^{-3}$ , for which the free-fall timescale is  $t_{\text{ff}} \lesssim 2.5 \times 10^2$  years. The migration timescale is therefore also of the order of the local free-fall timescale in our calculations. The rapid inward migration of the fragments in gravitationally unstable disks is also commonly seen in simulations of present-day star and planet formation (e.g., Vorobyov & Basu 2006; Baruteau et al. 2011; Machida et al. 2011; Zhu et al. 2012). These studies show that rapid migration occurs roughly over the so-called type I migration timescale

$$t_{\text{mig,I}} = \frac{h^2}{4C\mu q} \frac{2\pi}{\Omega} \quad (28)$$

(Tanaka et al. 2002), where  $C = 2.7 + 1.1\xi$ ,  $\xi$  is the

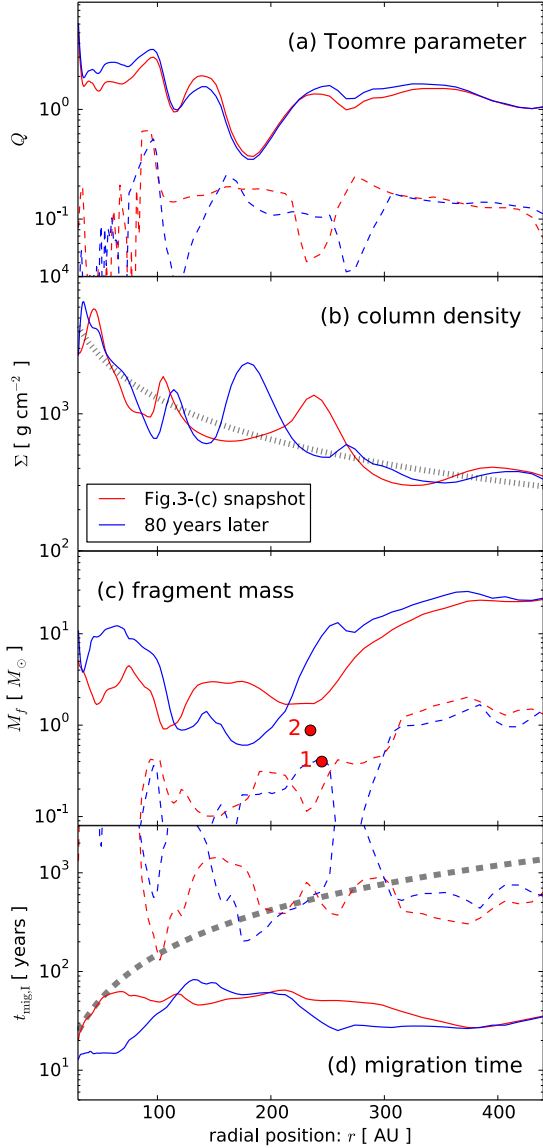


FIG. 23.— Radial distributions of physical quantities for the circumstellar disks shown in Figure 22: (a) Toomre  $Q$ -parameter, (b) vertical column density  $\Sigma$ , (c) fragment mass  $M_f$  (equation 29), and (d) type I migration timescale (equation 28). In each panel, the red curves pertain to the evolutionary state depicted in Figure 3-(c) and Figure 22-(a), whereas the blue curves correspond to 80 years later (see Figure 22-(b)). These two epochs are also displayed in Figure 24. In each panel, solid curves depict quantities averaged over the azimuthal  $\phi$  direction. The dashed lines in panel (a) represent the minimum values  $Q_{\min}(r)$  in an annulus of radius  $r$ , which roughly trace the  $Q$  values through either spiral arms or fragments. In panel (b), the thick dotted line shows the profile  $\Sigma \propto r^{-1}$  for reference. The colored dashed lines in panels (c) and (d) represent the minimum values of the estimated fragment mass and corresponding migration timescale in the annulus of radius  $r$ . In panel (c), the red filled circles indicate the masses of the two fragments marked in Figure 22-(a). In panel (d), we also plot the Kepler orbital period  $P_{\text{Kepler}} = 2\pi\sqrt{r^3/GM_*}$  for  $M_* = 45.4 M_\odot$  with a black dashed line.

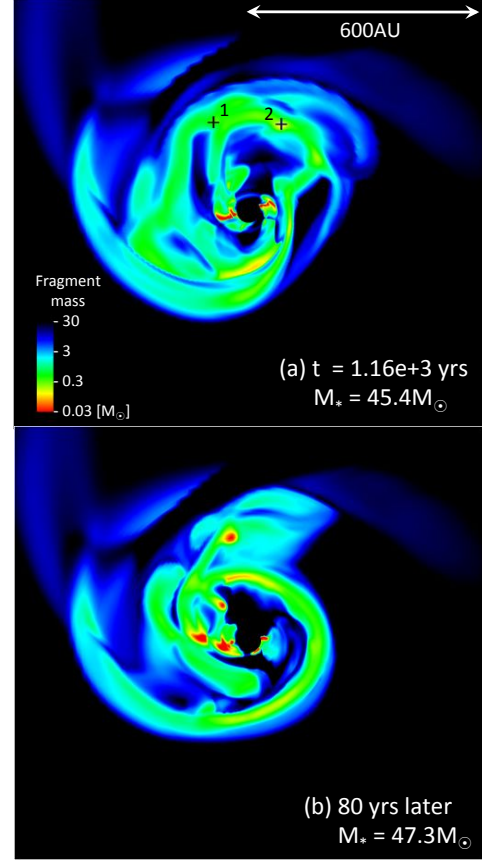


FIG. 24.— Same as Figure 22 but for the fragment masses evaluated locally with equation (29). In panel (a), we only mark the positions of the two fragments referred to in Figures 22 and 23 for this epoch.

radial gradient of the column density  $\Sigma \propto r^{-\xi}$ ,  $h$  is the disk aspect ratio,  $\mu = \pi\Sigma r^2/M_*$ , and  $q = M_f/M_*$ , where  $M_f$  is the fragment mass. Figure 23-(b) shows that the column density profile in our disk is well approximated by  $\Sigma \propto r^{-1}$ , i.e.,  $\xi = 1$ . The fragment mass  $M_f$  is approximated by the mass enclosed within a spatial scale of the most unstable wavelength  $\lambda = 2c_s^2/G\Sigma$ ,

$$M_f = \pi(\lambda/2)^2\Sigma = \frac{\pi c_s^4}{G^2\Sigma}. \quad (29)$$

Figure 23-(c) shows that the  $\phi$ -averaged fragment masses estimated by equation (29) span the range from  $\sim 1 M_\odot$  to several  $10 M_\odot$ . Because there are large density fluctuations in the disk, the locally-estimated fragment mass varies considerably. Figure 24 shows  $M_f \sim 0.1 - 1 M_\odot$  along the spiral arms, where the fragmentation often occurs. We also directly calculate the masses of the two fragments seen in Figure 22-(a) (marked as 1 and 2), by summing up the masses in the cells with the column density higher than  $5000 \text{ g cm}^{-2}$  around each fragment. The resulting values,  $M_{f1} \simeq 0.4 M_\odot$  and  $M_{f2} \simeq 0.9 M_\odot$ , are in rough agreement with the estimated values in Figure 24 (see also Figure 23-(c)).

In Figure 23-(d), we plot the type I migration timescale given by equation (28). Considering the fragment masses discussed above, we estimate that the corresponding mi-

gration timescales should be around  $\sim 100$  years, which are shorter than or comparable to the Kepler orbital periods. The rapid inward migration seen in our simulations can be well explained by the above evaluation. In addition to the two infalling fragments shown in Figures 3-(c) and 22, several similar events were observed during the simulation duration of  $10^3$  years. Some of the accretion bursts seen in Figure 21, although not all, are caused by such events.

As mentioned earlier, we have also performed quadruple resolution simulations with different numerical parameters. For case B-NF-HR4-m20-fc, for instance, we adopt  $f_{\text{limit}} = 24$  instead of the fiducial value  $f_{\text{limit}} = 12$ , where  $f_{\text{limit}}$  sets the cooling limit threshold (equation 10). As described in Section 2.1.2, a larger value for  $f_{\text{limit}}$  sets a more stringent limit on cooling. Figure 21 shows that the evolution for this case is quite similar to that for the double resolution case B-NF-HR2-m0, verifying that the resolution dependences examined above really come from the more efficient cooling allowed with higher resolution. For case B-NF-HR4-m20-lsk, on the other hand, we adopt a larger sink  $r_{\text{min}} = 52$  AU instead of the fiducial value  $r_{\text{min}} = 30$  AU. The stellar mass growth history for this case roughly traces that for case B-NF-HR4-m20, although with less variable accretion rates. The shortest timescale of accretion variability is roughly given by the Kepler orbital timescale near the radial inner boundary at  $r = r_{\text{min}}$ .

#### 4.3.2. Stellar UV Feedback with Variable Accretion

Next we investigate the effects of varying the grid resolution for evolutionary stages when UV feedback becomes important. For this purpose, we take case C (see Section 4.2.2) as the basis for comparison. Unlike case B considered above, UV feedback operates earlier and at lower stellar masses for case C (e.g., Figs. 4 and 5). This enables us to follow the evolution with UV feedback for a longer period of time at a reasonable computational cost. We double the resolution for the initial configuration,  $M_* = 0 M_\odot$ , and follow the evolution for  $5.5 \times 10^4$  years (case C-HR2).

Figure 25 displays the stellar mass (a) accretion rate (b), stellar radius (c), and UV emissivity (d) as a function of time for both case C and C-HR2. In agreement with what we have shown in Section 4.3.1, the accretion rate is more highly variable at the higher resolution (Fig. 25-b). After the different accretion histories over  $5.5 \times 10^4$  years, however, the final masses differ only by  $\sim 10\%$ . This is because the current evolutionary timescale is much longer than the local Kepler timescale within the disk (equation 19), so that we are no longer considering the short term evolution of a nearly isolated disk; the mass supply from the envelope ultimately controls stellar growth via mass accretion through the disk. Since the stellar radius abruptly changes with the variable mass accretion, the UV emissivity also displays very large fluctuations (Fig. 25-c, d). With the doubled resolution, the protostellar bloating and subsequent KH contraction are repeated several times because of multiple accretion bursts. The extinction and re-formation of bipolar HII regions also occurs accordingly. In comparison with the original case C, UV feedback begins to limit stellar mass growth earlier at  $M_* \simeq 100 M_\odot$ , but the star nevertheless accretes a larger amount of gas ( $\simeq 150 M_\odot$ )

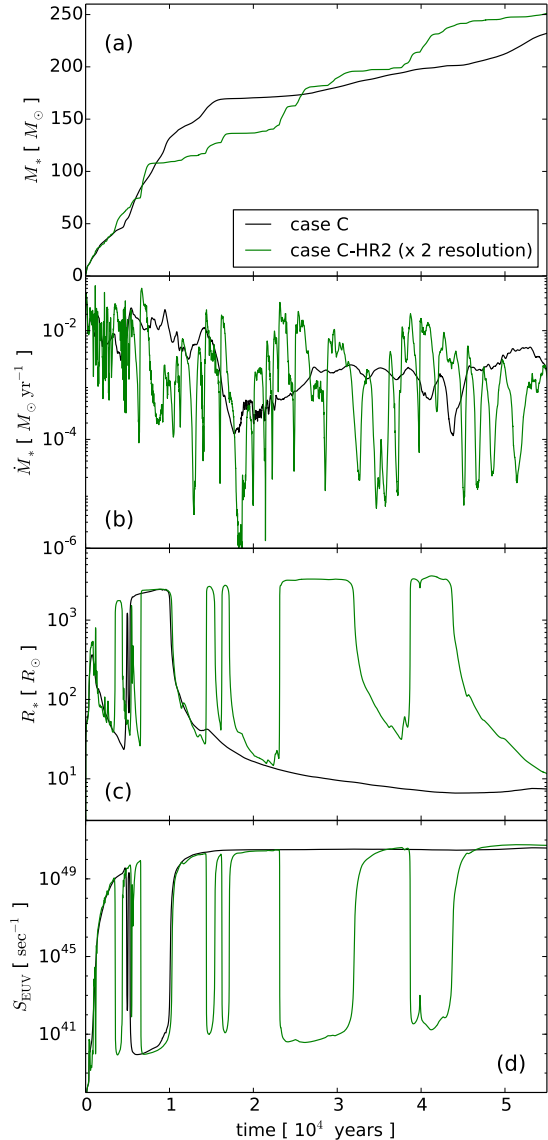


FIG. 25.— Effects of doubling the spatial resolution for a long-term evolution under the influence of UV feedback for case C. The evolution of (a) stellar mass, (b) accretion rate, (c) stellar radius, and (d) emissivity of ionizing photons is presented. In each panel, the black and green lines represent the fiducial case C and a test case with 2 times higher spatial resolution, C-HR2 (also see Table 1).

after the onset of significant UV feedback. The overall result is a slightly higher stellar mass at the end of the simulation than for the original case C.

## 5. DISCUSSION

### 5.1. Impact of Dissociation Feedback

As described in Section 4.2.1, the accretion limiting effect of stellar dissociating (FUV) radiation is modest in our simulations; FUV feedback slightly reduces mass accretion onto the star, but does not completely stop it, as opposed to ionizing (EUV) feedback (Figs. 8 and 9). This is in contrast to the conclusions of Susa (2013) and Susa et al. (2014), who show that mass accretion can be halted by FUV feedback alone. EUV feedback is not included in their SPH/N-body simulations because of

the limited spatial resolution, especially in polar regions where an HII region should first appear. To examine the roles of FUV feedback for our simulations in comparison with theirs, we return to our case D-DF, for which EUV feedback had been artificially turned off.

As described in Susa (2013), a circumstellar disk of density  $n \gtrsim 10^{11} \text{ cm}^{-3}$  is ultimately dispersed by FUV feedback in their simulations. This is because  $\text{H}_2$  formation heating mainly due to the three-body reaction efficiently heats the gas when the dense gas ( $n \gtrsim 10^{10} \text{ cm}^{-3}$ ) is exposed to FUV radiation. As the disk disperses, the gas density around stars rapidly falls to  $n \lesssim 10^7 \text{ cm}^{-3}$ , resulting in low accretion rates onto the stars. For our case D-DF, however, FUV radiation heats up the gas primarily in the polar regions throughout the course of  $8 \times 10^4$  years evolution. The dense disk with  $n \gtrsim 10^{11} \text{ cm}^{-3}$  survives in our case D-DF simulation, being protected against the FUV radiation by efficient  $\text{H}_2$  self-shielding in the inner regions of the disk. The pressure excess in the polar PDR is much less than what an HII region can provide when stellar EUV radiation is present. Unlike the effects of EUV feedback, the pressure structure in the envelope is hardly modified outside the PDR. Therefore mass accretion onto the disk continues from the envelope as well as from the disk onto the star with little modification by FUV feedback.

It seems that the disagreement outlined above stems from different efficiencies of  $\text{H}_2$  self-shielding in the vicinity of the star. Both simulations suffer from the inability to exactly model this effect in the innermost regions  $r \lesssim 30 \text{ AU}$ , currently masked by the sink. Numerical simulations devoted to resolving small-scale structure near the stellar surface will be needed in the future.

### 5.2. Formation of Binary and Multiple Stellar Systems

Our current simulations do not show clear indications for the formation of binary or multiple stellar systems. As explained in Section 4.3, disks will readily fragment, especially in simulations with high spatial resolution, but fragmentation actually enhances angular momentum transport in the disk and mass accretion onto the central stars via tidal torques and the rapid inward migration of the fragments. This is in disagreement with recent simulations claiming the formation of multiple stellar systems (see Section 1).

First of all, our inability to form binary and multiple stellar systems may be partly due to a selection bias; we did not choose primordial clouds that have strongly asymmetric or complex structure as starting configurations. Among HR14’s cosmological sample, for instance, some clouds have multiple density peaks emerging before the formation of embryo protostars (see also Turk et al. 2009). With typical separations of  $0.1 - 1 \text{ pc}$ , they may evolve to form wide-binary systems. We note that the number fraction of such clouds is only  $\simeq 5\%$  among 110 clouds.

On the other hand, more compact (e.g.,  $\lesssim 10^3 \text{ AU}$ ) binary or multiple stellar systems could form via disk fragmentation. Whereas a number of the fragments migrate inward to fall onto the star, some could potentially survive orbiting around the star or even as ejecta via gravitational interactions with other fragments. Our numerical method using the spherical coordinates and a stationary central sink *does* allow the formation of such systems. In

fact, Vorobyov & Basu (2015) report finding such events in their simulations using the similar numerical settings. We cannot discount the potential claim that, had we followed the long-term evolution at sufficiently high spatial resolution, we might also observe such events in our cases (e.g., Stacy & Bromm 2013). However, Vorobyov & Basu (2015) also point out that the ejection events are much rarer than the burst accretion events initiated by the migration of fragments. If the fragments grow to become massive stars emitting a copious amount of UV photons, then our current framework will have the limitation of not dealing with the multiple light sources.

It is also possible that binary or multiple stellar systems could form within our 30 AU sink. For present-day massive star formation, close binaries are the rule rather than the exception (e.g., Zinnecker & Yorke 2007). For example, the brightest Trapezium star, Ori  $\Theta^1\text{C}$  has components “1” and “2” separated by  $\sim 10 \text{ AU}$ . One of the binary components of the second brightest star, Ori  $\Theta^1\text{A1}$ , is itself a spectroscopic binary with a 1 AU separation. Ori  $\Theta^1\text{E}$  and Ori  $\Theta^1\text{B1}$  are also spectroscopic binaries with separations  $\sim 0.2 \text{ AU}$  and  $\sim 0.13 \text{ AU}$ . Ori  $\Theta^1\text{D}$  is a binary with a  $\sim 10 \text{ AU}$  separation. All in all, the Trapezium has at least 14 close components in 5 multiple stellar systems. If such systems are also common among primordial stars, close binary BH systems could form after a common envelope phase and eventually merge emitting gravitational waves. Interestingly, the recent detection GW150914 reported by Abbott et al. (2016) may really represent the signature of primordial close binaries (Kinugawa et al. 2014).

In general, the formation efficiency of binary or multiple systems depends on the production and survival rates of the fragments and perhaps on fission of rapidly rotating protostars, of which we know very little. As demonstrated in Section 4.3, the fragmentation rates in our simulations clearly depend on the spatial resolution used to follow the long-term evolution. Machida & Doi (2013) investigate the spatial resolution necessary to capture disk fragmentation with numerical convergence, meaning that the results no longer depend on the resolution. They conclude that numerical codes need to resolve structure at least down to the scale  $\sim 0.01 - 0.1 \text{ AU}$  (see their Appendix). Greif et al. (2012) show that about 1/3 of the emerging fragments survive in their simulations when they resolve such small scales without using the sink technique, although only the very early evolution for  $\sim 10$  years could be followed. Note that even these studies may suffer from limited spatial resolution; the numbers of cells assigned per Jeans length are 8 and 32 in Machida & Doi (2013) and Greif et al. (2012), respectively, whereas it is known that significantly higher resolution is required to also capture the turbulent motions expected in the early collapse stage (e.g., Turk et al. 2012).

We conclude that with current computational capabilities it is necessary to use sink cells or sink particles to follow the long term evolution up to the point that UV feedback becomes important. For such cases, disk fragmentation and the resulting stellar multiplicity will necessarily depend on the adopted spatial resolution. Stellar multiplicity should affect the evolution. Susa (2013) allow the creation of multiple sink (star) particles with-

out further mergers, and show that UV feedback from multiple protostars jointly halt the mass accretion. This fundamentally different implementation of sinks may explain why Susa et al. (2014) find no correlation between the final stellar masses and cloud-scale infall rates, in contrast to our results (see Section 4.2.3).

The evolution of the stellar radius is important for determining merger rates with other stars or fragments as well as the associated UV emissivities. Once the protostar inflates entering the supergiant stage after an accretion burst event, the large stellar size will further enhance the merger rates of nearby fragments and close companions. If a supergiant protostar is in a close binary system, for example, mass exchange with the companion star could cause the companion to inflate and initiate common envelope evolution of the primary and companion stars. As a protostar inflates, it can consume the gas in the inner parts of the circumstellar accretion disk, enhancing the instantaneous accretion rate even more. These processes can help the formation of very massive stars, in addition to the intermittent UV feedback shown in Section 4.2.2.

### 5.3. Effects of Magnetic Fields

We have not included effects of magnetic fields in our current simulations. However, theoretical studies predict that the field strength can be significantly amplified by the turbulent dynamo process during early collapse (e.g., Schleicher et al. 2010; Turk et al. 2012). Magnetic fields could affect the evolution in the late accretion stage in a number of ways. The turbulent motion in accretion disks can further increase the field strength and add to the magnetic pressure support of the disk (e.g., Tan & Blackman 2005). The angular momentum of the accreting material can be reduced by magnetic breaking (e.g., Machida & Doi 2013). Both effects could potentially suppress disk fragmentation. Nevertheless, some accretion variability should remain as long as the gravitational torque controls the mass and angular momentum transfer in disks.

Magnetically-driven outflows might appear intermittently with the variable mass accretion (e.g., Machida et al. 2011; Machida & Hosokawa 2013). It is interesting to speculate on the potential interaction between the stellar UV and outflow feedback mechanisms. Whereas the UV feedback is turned off by burst accretion (Section 4.2.2), the outflow power will be enhanced because a fraction of the accreting gas is generally diverted into the outflow (e.g., Matzner & McKee 1999). The UV and outflow feedback mechanisms may actually complement each other; the outflow is relatively weak as an HII region expands, and the outflow is activated as the HII region disappears. Future numerical simulations such as those performed for the present-day high-mass star formation (e.g., Kuiper et al. 2015) will explore these effects.

### 5.4. Signatures of Primordial Stars in Galactic Metal-poor Stars

Although only a handful cases were studied above, it would be useful to confront our results with current observational constraints on the masses of primordial stars. Figure 19-(a) includes the recently estimated masses of Pop III supernova progenitors derived from abundance

patterns in Galactic metal-poor stars. Caffau et al. (2011), Keller et al. (2014), and Frebel et al. (2015) have shown that the abundance patterns of extremely metal-poor ( $[\text{Fe}/\text{H}] < -4$ ) stars can be explained by chemical yields of core collapse supernovae (CCSN), whose progenitors are several  $\times 10 M_{\odot}$  stars. Among our simulations, such ordinary massive stars ultimately form for cases D and E, after the UV feedback efficiently shuts off mass accretion (Section 4.2.1).

Aoki et al. (2014) recently found a peculiar abundance pattern in SDSS J001820.5-093939.2, which does not match the yields of CCSN but seems to indicate the existence of more massive populations: progenitors of pair-instability supernovae (PISN;  $120 M_{\odot} \lesssim M_{*} \lesssim 240 M_{\odot}$ , e.g., Yoon et al. 2012) or the core-collapse of very massive stars ( $M_{*} \gtrsim 240 M_{\odot}$ , e.g., Ohkubo et al. 2009). For our cases A–C, the very massive stars above the PISN range form due to the process of intermittent (burst) accretion and its associated variability of UV feedback (Section 4.2.2). Although currently absent among the five cases considered here, we strongly suspect that we would also have formed stars in the PISN range, if a greater number of cases had been considered. Figure 19 suggests that such stars will appear for the cases that have the cloud-scale infall rates between the values for cases A and C. However, Aoki et al. (2014) actually show that such very massive stars may be preferred to the PISN progenitors to explain the peculiar abundance pattern. Note that this object has a higher metallicity  $[\text{Fe}/\text{H}] \simeq -2.5$  than the above mentioned very metal-poor stars. A higher metallicity is expected theoretically, because even a single massive explosion will elevate the metallicity of the polluted gas to this level (Karlsson et al. 2008). Our results indicate that  $M_{*} \gtrsim 100 M_{\odot}$  primordial stars constitute a majority (Fig. 19), so it might be possible to find similar signatures in other nearby stars. However, this still may be challenging, because such energetic supernovae, could potentially expel most of the gas out of a halo and suppress subsequent star formation (Cooke & Madau 2014). It will be necessary to determine the star formation efficiency after energetic supernovae in order to assess the mass distribution of massive primordial stars using stellar archaeology.

### 5.5. Formation of Supermassive Stars: an Extreme Case

Several authors have considered the formation of primordial supermassive ( $M_{*} \sim 10^5 M_{\odot}$ ) stars (SMSs) as a promising pathway to seed supermassive BHs in the early universe (e.g., Bromm & Loeb 2003). A popular model supposes that such an extreme mode of primordial star formation should occur in the so-called atomic-cooling haloes exposed to strong FUV radiation. With only atomic hydrogen as an available coolant, the cloud collapse advances almost isothermally at a higher temperature ( $T \simeq 8000$  K) than for typical primordial cases (e.g., Omukai 2001). As a result, very rapid accretion and sufficient material (high Jeans mass) is expected to be available within the stellar lifetime of  $\sim \text{Myr}$ , during which the stellar mass could attain values  $\gtrsim 10^5 M_{\odot}$  (e.g., Regan & Haehnelt 2009; Latif et al. 2013; Inayoshi et al. 2014). Recent numerical simulations show that, also for such cases, circumstellar disks easily fragment due to the gravitational instability (e.g., Regan et al.

2014; Becerra et al. 2015). It is also expected that the emerging fragments will rapidly migrate inward through the disk (e.g., Inayoshi & Haiman 2014), as for normal Pop III cases (see Section 4.3.1). The resulting accretion rates will thus show significant variability.

As discussed above, stellar UV feedback will be very weak whenever the protostar enters the supergiant stage for accretion rates exceeding  $0.01 M_{\odot} \text{ yr}^{-1}$ . However, the protostar will contract toward the ZAMS under realistic conditions of variable accretion, each time the accretion rate falls below  $0.01 M_{\odot} \text{ yr}^{-1}$ . Stellar evolution calculations show that such a slowly accreting star can reach the ZAMS, if this lower rate of accretion continues for  $\gtrsim 10^3$  years (Sakurai et al. 2015). As it approaches the ZAMS, the stellar UV emissivity rises sharply, initiating very powerful UV feedback (Section 4.2.2). For the normal primordial cases studied above, a short burst of rapid mass accretion will cause the star to bloat up again and the star can again accrete more available material. Although case B has reached nearly  $600 M_{\odot}$  through this recurrent accretion process and is still accreting material after  $7 \times 10^4$  years, our simulations are still far from the mass  $10^5 M_{\odot}$  and average accretion rates  $0.1 M_{\odot} \text{ yr}^{-1}$  necessary to produce such an SMS within a Myr. Our newly developed SE-RHD numerical code will be useful to explore the interplay between variable accretion and UV feedback for the formation of SMSs.

Needless to say, other physical processes which have not been fully considered, such as stellar multiplicity (Section 5.2) and magnetic fields (Section 5.3), can also jointly modify the protostellar accretion histories. Since the formation of SMSs is an extreme version of the formation of very massive stars studied in Section 4.2.2, both cases share many common theoretical issues to be solved in future studies.

## 6. CONCLUSIONS

We have studied the long term evolution during the accretion stage of primordial star formation, focusing on the interplay between highly variable accretion onto the star and stellar UV feedback. To follow the evolution by numerical simulations, we have developed a new 3D SE-RHD hybrid code to solve for the radiation hydrodynamics of the accretion flow simultaneously with the stellar evolution of the accreting protostar. The evolution of the protostellar accretion flow under the influence of both ionizing (EUV) and photodissociating (FUV) radiative feedback has been followed for over  $\sim 10^5$  years. We have examined the evolution of five different primordial clouds in representative dark matter halos found in cosmological structure formation simulations. Many numerical parameters (e.g., spatial resolution, sink cell size) used in our simulations have been varied to assess their effects on the results. Our findings are summarized as follows:

1. The resulting stellar masses  $M_*$  show a great diversity:  $10 M_{\odot} \lesssim M_* \lesssim 10^3 M_{\odot}$ , which also has been inferred in previous studies (e.g., HR14, HR15; Susa et al. 2014). The stellar mass tends to be higher for clouds with a higher average infall rate, a cloud parameter set during the early collapse stage *before* the formation of an embryo protostar. This roughly agrees with our previous

findings discussed in HR14.

2. Ordinary massive ( $M_* \lesssim 100 M_{\odot}$ ) stars form in cases with relatively slow mass accretion. For these cases, UV feedback efficiently shuts off accretion once a protostar reaches the late KH contraction stage, as shown in our previous 2D studies. On the other hand, very massive ( $M_* \gtrsim 250 M_{\odot}$ ) stars also form when relatively rapid accretion is available. For such cases, the protostar goes through a “supergiant protostar” evolutionary stage, which recurrently appears with the highly variable mass accretion associated with self-gravitating circumstellar disks. As a result of the fluctuating stellar radius, characterized by alternating periods of contraction and inflation, the formation and extinction of HII regions also recur repeatedly. Over the course of time UV feedback only operates intermittently, and does not efficiently halt mass accretion onto the star.
3. Very massive stars form in three out of the five examined cases (and two of these three yield only lower limits to the final stellar masses). According to a statistical study by HR15, who have analyzed physical properties of more than 1500 primordial clouds, the formation of such very massive stars can be a major mode of primordial star formation.
4. According to our systematic assessment of varying the numerical parameters, our current simulations do not converge with increasing spatial resolution. As far as we can tell with our present suite of numerical tools, however, variable accretion and the resulting intermittent UV feedback becomes even more prominent at higher spatial resolution.

Our results show that the interplay between stellar UV feedback and variable mass accretion can help the formation of very massive primordial stars, making this a likely pathway to form a significant number of very massive stars in the early universe, circumventing potential barriers, such as stellar UV feedback and disk fragmentation. The peculiar abundance pattern recently discovered in a Galactic metal-poor star (Aoki et al. 2014) could be the observational signature indicative of such very massive stars. With the resolution dependence of our results discussed in Section 4.3, this basic proof of concept investigation still requires further detailed study to verify the above idea.

As an extension of cases considered here, the formation of even more massive (or supermassive) stars may be possible under certain favorable conditions; the feasibility of this scenario will be examined in future studies. Such studies will be necessary to determine the maximum mass of primordial stars, a key quantity when considering the origin of the supermassive black holes observed in the early universe.

The authors thank Hajime Susa, Eduard Vorobyov, Masayuki Umemura, Shu-ichiro Inutsuka, and Ken Nomoto for fruitful discussions and comments. The numerical simulations were performed on the Cray XC30 at the Center for Computational Astrophysics, CfCA, of



the National Astronomical Observatory of Japan. Portions of this work were conducted at the Jet Propulsion Laboratory, California Institute of Technology, operating under a contract with the National Aeronautics and Space Administration (NASA). This work was financially supported by the Grants-in-Aid for Basic Research by the Ministry of Education, Science and Culture of Japan (25800102, 15H00776: TH, 25287040: KO, 25287050: NY) and by Grant-in-Aid for JSPS Fellows (SH). RK acknowledges funding within the Emmy Noether Research Group on “Accretion Flows and Feedback in Realistic Models of Massive Star Formation” granted by the German Research Foundation (DFG) under grant no. KU 2849/3-1.

## REFERENCES

- Abbott, B. P., et al. 2016, *Physical Review Letters*, 116, 061102
- Abel, T., Anninos, P., Zhang, Y., & Norman, M. L. 1997, *New Astronomy*, 2, 181
- Abel, T., Bryan, G. L., & Norman, M. L. 2002, *Science*, 295, 93
- Aoki, W., Tominaga, N., Beers, T. C., Honda, S., & Lee, Y. S. 2014, *Science*, 345, 912
- Baruteau, C., Meru, F., & Paardekooper, S.-J. 2011, *MNRAS*, 416, 1971
- Bate, M. R., Lodato, G., & Pringle, J. E. 2010, *MNRAS*, 401, 1505
- Becerra, F., Greif, T. H., Springel, V., & Hernquist, L. E. 2015, *MNRAS*, 446, 2380
- Bromm, V., Coppi, P. S., & Larson, R. B. 2002, *ApJ*, 564, 23
- Bromm, V., & Loeb, A. 2003, *ApJ*, 596, 34
- Bromm, V., Yoshida, N., Hernquist, L., & McKee, C. F. 2009, *Nature*, 459, 49
- Caffau, E., et al. 2011, *Nature*, 477, 67
- Clark, P. C., Glover, S. C. O., & Klessen, R. S. 2012, *MNRAS*, 420, 745
- Clark, P. C., Glover, S. C. O., Smith, R. J., Greif, T. H., Klessen, R. S., & Bromm, V. 2011, *Science*, 331, 1040
- Cooke, R. J., & Madau, P. 2014, *ApJ*, 791, 116
- DeSouza, A. L., & Basu, S. 2015, *MNRAS*, 450, 295
- Draine, B. T., & Bertoldi, F. 1996, *ApJ*, 468, 269
- Federrath, C., Sur, S., Schleicher, D. R. G., Banerjee, R., & Klessen, R. S. 2011, *ApJ*, 731, 62
- Fielding, D. B., McKee, C. F., Socrates, A., Cunningham, A. J., & Klein, R. I. 2015, *MNRAS*, 450, 3306
- Forrey, R. C. 2013, *ApJ*, 773, L25
- Frebel, A., Chiti, A., Ji, A. P., Jacobson, H. R., & Placco, V. M. 2015, *ApJ*, 810, L27
- Galli, D., & Palla, F. 1998, *A&A*, 335, 403
- Greif, T. H. 2014, *MNRAS*, 444, 1566
- . 2015, *Computational Astrophysics and Cosmology*, 2, 3
- Greif, T. H., Bromm, V., Clark, P. C., Glover, S. C. O., Smith, R. J., Klessen, R. S., Yoshida, N., & Springel, V. 2012, *MNRAS*, 424, 399
- Greif, T. H., Springel, V., White, S. D. M., Glover, S. C. O., Clark, P. C., Smith, R. J., Klessen, R. S., & Bromm, V. 2011, *ApJ*, 737, 75
- Hartwig, T., Clark, P. C., Glover, S. C. O., Klessen, R. S., & Sasaki, M. 2015, *ApJ*, 799, 114
- Hirano, S., Hosokawa, T., Yoshida, N., Omukai, K., & Yorke, H. W. 2015, *MNRAS*, 448, 568
- Hirano, S., Hosokawa, T., Yoshida, N., Umeda, H., Omukai, K., Chiaki, G., & Yorke, H. W. 2014, *ApJ*, 781, 60
- Hirano, S., & Yoshida, N. 2013, *ApJ*, 763, 52
- Hollenbach, D., Johnstone, D., Lizano, S., & Shu, F. 1994, *ApJ*, 428, 654
- Hosokawa, T., & Omukai, K. 2009, *ApJ*, 691, 823
- Hosokawa, T., Omukai, K., & Yorke, H. W. 2012a, *ApJ*, 756, 93
- Hosokawa, T., Omukai, K., Yoshida, N., & Yorke, H. W. 2011, *Science*, 334, 1250
- Hosokawa, T., Yorke, H. W., Inayoshi, K., Omukai, K., & Yoshida, N. 2013, *ApJ*, 778, 178
- Hosokawa, T., Yorke, H. W., & Omukai, K. 2010, *ApJ*, 721, 478
- Hosokawa, T., Yoshida, N., Omukai, K., & Yorke, H. W. 2012b, *ApJ*, 760, L37
- Inayoshi, K., & Haiman, Z. 2014, *MNRAS*, 445, 1549
- Inayoshi, K., Omukai, K., & Tasker, E. 2014, *MNRAS*, 445, L109
- Ishigaki, M. N., Tominaga, N., Kobayashi, C., & Nomoto, K. 2014, *ApJ*, 792, L32
- John, T. L. 1988, *A&A*, 193, 189
- Karlssohn, T., Johnson, J. L., & Bromm, V. 2008, *ApJ*, 679, 6
- Keller, S. C., et al. 2014, *Nature*, 506, 463
- Kinugawa, T., Inayoshi, K., Hotokezaka, K., Nakauchi, D., & Nakamura, T. 2014, *MNRAS*, 442, 2963
- Kreckel, H., Bruhns, H., Čížek, M., Glover, S. C. O., Miller, K. A., Urbain, X., & Savin, D. W. 2010, *Science*, 329, 69
- Kuiper, R., Klahr, H., Beuther, H., & Henning, T. 2010a, *ApJ*, 722, 1556
- . 2011, *ApJ*, 732, 20
- Kuiper, R., Klahr, H., Dullemond, C., Kley, W., & Henning, T. 2010b, *A&A*, 511, A81
- Kuiper, R., & Klessen, R. S. 2013, *A&A*, 555, A7
- Kuiper, R., & Yorke, H. W. 2013, *ApJ*, 772, 61
- Kuiper, R., Yorke, H. W., & Turner, N. J. 2015, *ApJ*, 800, 86
- Latif, M. A., Schleicher, D. R. G., Schmidt, W., & Niemeyer, J. 2013, *MNRAS*, 433, 1607
- Levermore, C. D., & Pomraning, G. C. 1981, *ApJ*, 248, 321
- Machida, M. N., & Doi, K. 2013, *MNRAS*, 435, 3283
- Machida, M. N., & Hosokawa, T. 2013, *MNRAS*, 431, 1719
- Machida, M. N., Inutsuka, S.-i., & Matsumoto, T. 2011, *ApJ*, 729, 42
- Martin, P. G., Schwarz, D. H., & Mandy, M. E. 1996, *ApJ*, 461, 265
- Matzner, C. D., & McKee, C. F. 1999, *ApJ*, 510, 379
- McKee, C. F., & Tan, J. C. 2008, *ApJ*, 681, 771
- Meece, G. R., Smith, B. D., & O'Shea, B. W. 2014, *ApJ*, 783, 75
- Mignone, A., Bodo, G., Massaglia, S., Matsakos, T., Tesileanu, O., Zanni, C., & Ferrari, A. 2007, *ApJS*, 170, 228
- Millar, T. J. 1991, *A&A*, 242, 241
- Oh, S. P., & Haiman, Z. 2002, *ApJ*, 569, 558
- Ohkubo, T., Nomoto, K., Umeda, H., Yoshida, N., & Tsuruta, S. 2009, *ApJ*, 706, 1184
- Omukai, K. 2001, *ApJ*, 546, 635
- Omukai, K., & Inutsuka, S.-i. 2002, *MNRAS*, 332, 59
- Omukai, K., & Nishi, R. 1998, *ApJ*, 508, 141
- Omukai, K., & Palla, F. 2003, *ApJ*, 589, 677
- O'Shea, B. W., McKee, C. F., Heger, A., & Abel, T. 2008, in *American Institute of Physics Conference Series*, Vol. 990, First Stars III, ed. B. W. O'Shea & A. Heger, D13
- O'Shea, B. W., & Norman, M. L. 2008, *ApJ*, 673, 14
- Osterbrock, D. E., & Ferland, G. J. 2006, *Astrophysics of gaseous nebulae and active galactic nuclei*, ed. Osterbrock, D. E. & Ferland, G. J.
- Palla, F., Salpeter, E. E., & Stahler, S. W. 1983, *ApJ*, 271, 632
- Palla, F., & Stahler, S. W. 1992, *ApJ*, 392, 667
- Papaloizou, J. C. B., & Terquem, C. 1995, *MNRAS*, 274, 987
- Peters, T., Klessen, R. S., Mac Low, M.-M., & Banerjee, R. 2010, *ApJ*, 725, 134
- Regan, J. A., & Haehnelt, M. G. 2009, *MNRAS*, 396, 343
- Regan, J. A., Johansson, P. H., & Haehnelt, M. G. 2014, *MNRAS*, 439, 1160
- Richling, S., & Yorke, H. W. 1997, *A&A*, 327, 317
- Sakurai, Y., Hosokawa, T., Yoshida, N., & Yorke, H. W. 2015, *MNRAS*, 452, 755
- Schleicher, D. R. G., Banerjee, R., Sur, S., Arshakian, T. G., Klessen, R. S., Beck, R., & Spaans, M. 2010, *A&A*, 522, A115
- Schleicher, D. R. G., Palla, F., Ferrara, A., Galli, D., & Latif, M. 2013, *A&A*, 558, A59
- Schneider, R., Omukai, K., Limongi, M., Ferrara, A., Salvaterra, R., Chieffi, A., & Bianchi, S. 2012, *MNRAS*, 423, L60
- Shakura, N. I., & Sunyaev, R. A. 1973, *A&A*, 24, 337
- Siess, L., Forestini, M., & Bertout, C. 1997, *A&A*, 326, 1001
- Smith, R. J., Hosokawa, T., Omukai, K., Glover, S. C. O., & Klessen, R. S. 2012, *MNRAS*, 424, 457
- Springel, V. 2005, *MNRAS*, 364, 1105
- Stacy, A., & Bromm, V. 2013, *MNRAS*, 433, 1094
- Stacy, A., Greif, T. H., & Bromm, V. 2010, *MNRAS*, 403, 45
- . 2012, *MNRAS*, 2508
- Stahler, S. W., Palla, F., & Salpeter, E. E. 1986, *ApJ*, 302, 590
- Stahler, S. W., Shu, F. H., & Taam, R. E. 1980, *ApJ*, 241, 637
- Susa, H. 2013, *ApJ*, 773, 185
- Susa, H., Hasegawa, K., & Tominaga, N. 2014, *ApJ*, 792, 32
- Tan, J. C., & Blackman, E. G. 2005, *MNRAS*, 362, 983
- Tan, J. C., & McKee, C. F. 2004, *ApJ*, 603, 383
- Tanaka, H., Takeuchi, T., & Ward, W. R. 2002, *ApJ*, 565, 1257
- Tanaka, K. E. I., Nakamoto, T., & Omukai, K. 2013, *ApJ*, 773, 155
- Tielens, A. G. G. M., & Hollenbach, D. 1985, *ApJ*, 291, 722
- Truelove, J. K., Klein, R. I., McKee, C. F., Holliman, II, J. H., Howell, L. H., & Greenough, J. A. 1997, *ApJ*, 489, L179
- Turk, M. J., Abel, T., & O'Shea, B. 2009, *Science*, 325, 601
- Turk, M. J., Oishi, J. S., Abel, T., & Bryan, G. L. 2012, *ApJ*, 745, 154
- Vorobyov, E. I., & Basu, S. 2006, *ApJ*, 650, 956
- . 2015, *ApJ*, 805, 115
- Vorobyov, E. I., DeSouza, A. L., & Basu, S. 2013, *ApJ*, 768, 131
- Whalen, D., & Norman, M. L. 2008, *ApJ*, 673, 664

Table A1. Ideal Cases for Homogeneous Clouds Considered

Cases	$N_R \cdot N_\theta \cdot N_\phi$	$\Delta t$ ( $10^4$ yr)	$M_*(M_\odot)$
HM2D	$64 \cdot 16 \cdot 1$	5	59.8
HM2D-NF <sup>†</sup>	$64 \cdot 16 \cdot 1$	5	
HM	$64 \cdot 16 \cdot 64$	3	70.8
HM-ssk <sup>•</sup>	$64 \cdot 16 \cdot 64$	2.6	71.1
HM-HR2 <sup>†</sup>	$128 \cdot 32 \cdot 128$	2.6	69.0

Col. 2: numbers of grid cells, Col. 3: time duration of simulations. Col. 4: final stellar masses. The radial outer boundary is at  $r_{\max} = 4 \times 10^4$  AU, symmetry is assumed with respect to the equatorial plane ( $\theta = 0$ ), and the initial cloud mass is  $157 M_\odot$  for all cases.

<sup>†</sup>: The suffixes have the same meanings as in Table. 1.

<sup>•</sup>: Smaller sink with  $r_{\min} \simeq 10$  AU ( $r_{\min} = 30$  AU for the other cases).

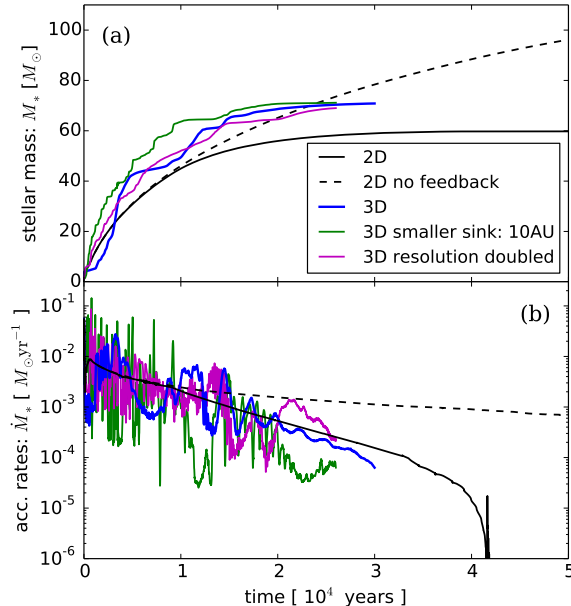


FIG. A1.— Evolution of the stellar mass (panel a) and accretion rates (panel b) for test cases starting with a homogeneous cloud (Table A1). The black solid and dashed lines represent the 2D axisymmetric cases with (HM2D) and without (HM2D-NF) UV feedback. The other lines represent 3D cases with different numerical settings: the fiducial case HM (blue), HM-ssk with a smaller sink (green), and HM-HR2 with doubled spatial resolution (magenta). The origin of time ( $t = 0$ ) marks the epoch of stellar birth after the runaway cloud collapse.

Yoon, S.-C., Dierks, A., & Langer, N. 2012, *A&A*, 542, A113  
 Yorke, H. W., & Bodenheimer, P. 2008, in *Astronomical Society of the Pacific Conference Series*, Vol. 387, *Massive Star Formation: Observations Confront Theory*, ed. H. Beuther, H. Linz, & T. Henning, 189  
 Yoshida, N., Abel, T., Hernquist, L., & Sugiyama, N. 2003, *ApJ*, 592, 645

Yoshida, N., Omukai, K., & Hernquist, L. 2007, *ApJ*, 667, L117  
 —. 2008, *Science*, 321, 669  
 Yoshida, N., Omukai, K., Hernquist, L., & Abel, T. 2006, *ApJ*, 652, 6  
 Zhu, Z., Hartmann, L., Nelson, R. P., & Gammie, C. F. 2012, *ApJ*, 746, 110  
 Zinnecker, H., & Yorke, H. W. 2007, *ARA&A*, 45, 481

## APPENDIX

### A. IDEAL TEST CASES WITH A HOMOGENEOUS CLOUD

In addition to the cosmological cases studied above, we also perform simulations starting with idealized initial conditions: a zero-metallicity homogeneous gas cloud with the initial density  $\rho_0 = 3.5 \times 10^{-19} \text{ cm}^{-3}$ , temperature  $T_0 = 200$  K, and chemical compositions  $X_{\text{H}_2} = 5 \times 10^{-3}$ ,  $X_{\text{e}} = X_{\text{HII}} = 10^{-4}$ , where  $X_i$  is the number ratio between the species  $i$  and hydrogen nuclei. We assume that the cloud is initially rigidly rotating at an angular velocity  $\Omega_0 = 4 \times 10^{-14} \text{ Hz}$ , which is about 13 % of the Kepler value for the enclosed gas mass  $\sqrt{GM(< r)/r^3} = \sqrt{4\pi G\rho_0/3}$ , independent of radius  $r$ . Since the initial Jeans length  $\simeq 3 \times 10^4$  AU is smaller than the cloud's radial extension  $4 \times 10^4$  AU, the cloud begins to gravitationally collapse in the well-known self-similar fashion (e.g., Omukai & Nishi 1998). For the current test cases, we use our modified version of the mesh-based PLUTO code from the beginning, unlike the cosmological cases for which the N-body/SPH code GADGET-2 had been used for the early collapse stage (see Section 2). The grid configuration is almost the same as described in Section 2, except that the current computational domain assumes mirror symmetry with respect to the equator throughout the evolution. We follow the collapse without a central sink cell until the central density reaches  $\sim 10^{12} \text{ cm}^{-3}$  and the minimum Jeans length becomes

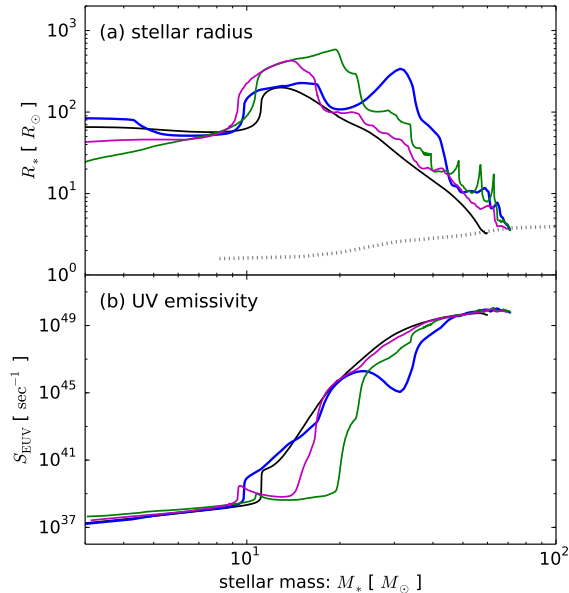


FIG. A2.— Evolution of the stellar radius (panel a) and ionizing (EUV) photon emissivity (panel b) for the test cases starting with a homogeneous cloud. The different lines represent the same cases as in Figure A1. In panel (a), the dotted line shows the mass-radius relationship for zero-age main-sequence stars.

poorly resolved. We then introduce the sink cell to follow the subsequent evolution in the protostellar accretion stage using either 2D or 3D versions of our SE-RHD hybrid code.

For all examined 3D cases, the evolution is similar to that obtained for the cosmological cases D and E (see Section 4.2.1);  $M_* \simeq 60 - 70 M_\odot$  stars form after UV feedback caused by an expanding bipolar HII region efficiently halts mass accretion. For the 2D cases we used a so-called  $\alpha$ -viscosity with  $\alpha = 1.0$  to enable angular momentum transport under axial symmetry (e.g., Kuiper et al. 2011). Similarly, the evolution of stellar mass growth with and without UV feedback, HM2D and HM2D-NF (Fig. A1), is comparable to that seen in our previous 2D SE-RHD simulations in HS11, although a different hybrid code was used. UV feedback begins to operate for  $M_* \gtrsim 40 M_\odot$  as the UV emissivity rises in the late KH contraction stage (Fig. A2). The 3D cases show a comparable evolution, except for the large fluctuations of accretion rates seen in Figure A1-(b). This is due to the manner of mass and angular momentum transport in self-gravitating circumstellar disks. We note that, for these idealized 3D cases, the assumed initial axial symmetry is well preserved until the disk begins to grow during the accretion stage. Thus, even with a much less disturbed structure of the accretion envelope than for our cosmological cases, highly variable accretion occurs in general. Since, however, the mean accretion rate is relatively low for these test cases, the protostar continues to contract to the ZAMS without being brought to the supergiant stage by accretion bursts. This is still the same even with the doubled spatial resolution (case HM-HR2), though the scatter of the accretion rates is larger than the fiducial case HM, as analogously seen for cosmological cases B and C (Section 4.3).

For the above cases, the stellar radius is always much smaller than the default sink size 30 AU. We thus also examine the effects of reducing the sink size to 10 AU (case HM-ssk). Figure A1 shows that the resulting accretion history is more variable with the smaller sink. This trend is also consistent with our findings for cosmological case B, for which a larger sink resulted in less accretion variability (Fig. 21). Although the stellar mass growth is even more rapid than for the other 3D cases for the first  $10^4$  years (Fig. A1-a), UV feedback limits the mass accretion once a bipolar HII region begins to expand. Since the 10 AU sink is still larger than the stellar radius, we still need further studies dedicated to resolving the flow connecting the disk inner edge and stellar surface. It is also possible that tight binaries with separations much smaller than  $\sim 10$  AU might form as seen in the Galaxy (Section 5.2), whose formation mechanism is poorly understood.